Precambrian Research 395 (2023) 107132

Contents lists available at ScienceDirect

Precambrian Research

journal homepage: www.elsevier.com/locate/precamres

The unroofing of Archean crustal domes as recorded by detrital zircon and apatite

Anthony J.I. Clarke [a,*], Christopher L. Kirkland [a], Stijn Glorie [b], Jack Gillespie [c], Peter D. Kinny [c]

[a] Timescales of Mineral Systems Group, School of Earth and Planetary Sciences, Curtin University, GPO Box U1987, Perth, WA 6845, Australia
[b] Department of Earth Sciences, University of Adelaide, SA 5000, Australia
[c] The Institute for Geoscience Research (TIGeR), School of Earth and Planetary Sciences, Curtin University, Perth, Bentley, WA 6845, Australia

ARTICLE INFO

Keywords:
Pilbara Craton
LA–ICP–MS
Lu–Hf
Sm–Nd
U–Pb
West Australian Craton

ABSTRACT

This study presents *in-situ* U–Pb, Lu–Hf, and Sm–Nd isotopic data for detrital zircon and apatite collected from ephemeral streams of the East Pilbara Terrane, Western Australia. Given their disparate abundances in felsic versus mafic lithologies, a tandem apatite-zircon approach may offer more holistic insights into crust formation. Apatite U–Pb data define a single age peak at c. 2.9 Ga, consistent with labile, proximal, and first-cycle detritus from the Pilbara Craton. Conversely, zircon, a more refractory and durable mineral, records a more diverse geological history with U–Pb ages spanning from 3.6 to 0.2 Ga. The apatite age of c. 2.9 Ga records the timing through the Pb closure temperature during regional cooling following prograde metamorphism, while the Lu–Hf and Sm–Nd isotopic systems in the same grains yield c. 3.2 Ga isochrons, consistent with magmatic crystallisation at that time. Crystallisation age, initial $^{143}Nd/^{144}Nd$ and trace element geochemistry (Eu/Eu*) imply a chondritic or mixed (more radiogenic plus a less radiogenic) source for the apatite grains locally derived from the East Pilbara Terrane. Conversely, zircon εHf data reveal a broadly chondritic Paleoarchean proto-crust undergoing continual isotopic evolution punctuated by the input of juvenile, more radiogenic material on a quasiperiodic basis. Previous workers have invoked a crust-mantle overturn model triggered by stagnant-lid cooling and the episodic (re)fertilisation of the upper mantle to account for the periodic nature of crust formation in the East Pilbara Terrane. Detrital zircon grains track this process from a c. 3.8 Ga component that may have acted as a nucleus for subsequent crust formation. The oldest detrital zircon, on average, encompass less radiogenic (−ve εHf) components suggesting that the oldest grains preserve the unroofing of an ancient reworked crustal nucleus. Thus, the detrital zircon load arguably provides a more holistic record of the older crust in the region than the crystalline domes alone. Specifically, the less radiogenic dome cores are preferentially eroded due to their structural position and their mineral cargo lost into the detrital archive. We demonstrate that the apatite-zircon approach can be limited by the ability of apatite to be retained through crustal denudation.

1. Introduction

The continental crust is arguably the fundamental geochemical reservoir that shaped the evolution of Earth's atmosphere, oceans, biosphere, and ore deposits (Hawkesworth et al., 2020). With increasing age, the record of crustal evolution becomes increasingly fragmented due to an inevitable preservation bias in the rock record (Cawood et al., 2012, 2013; Hawkesworth et al., 2019). Hence, the detrital mineral archive may be an important store of information poorly retained in the crystalline rock record (Belousova et al., 2010; Cawood et al., 2012, 2013; Dhuime et al., 2017; Hawkesworth et al., 2019; Taylor and McLennan, 1985). Accordingly, detrital studies of resistive minerals have become commonplace in resolving questions regarding crustal formation (Cawood et al., 2013), orogenesis (Spencer et al., 2015), and source-to-sink relationships (Moecher and Samson, 2006).

The Lu–Hf signature in U–Pb dated zircon is an established tool to constrain crust-mantle differentiation and aids understanding of the timing, rate, and duration of continental crust formation and reworking (Belousova et al., 2010; Cawood et al., 2013). Although zircon crystals provide a wealth of information, they tend to crystallise from relatively evolved (SiO_2-rich) magmas (Moecher and Samson, 2006). This compositional effect has the potentially undesirable consequence of

* Corresponding author.
E-mail address: 20392091@student.curtin.edu.au (A.J.I. Clarke).

https://doi.org/10.1016/j.precamres.2023.107132
Received 20 January 2023; Received in revised form 23 June 2023; Accepted 3 July 2023
Available online 2 August 2023

biasing the zircon crustal growth record towards more silica-rich (felsic) lithologies (Malusà et al., 2016). Furthermore, each tectonic environment has a different degree of grain preservation potential, which may further bias the detrital zircon record (Barham et al., 2022; Cawood et al., 2013; Spencer et al., 2015). Rather than simply representing episodes of crust formation, peaks in the detrital zircon U–Pb record could instead be a function of the preservation potential of different tectonic environments (Barham et al., 2022; Cawood et al., 2013).

Apatite is increasingly used to complement the zircon record as it extends the source rock compositional envelope that is tracked and can be dated by a range of established [U–Pb; e.g. Chew et al. (2014)] and more novel [Lu–Hf; e.g. Simpson et al. (2021) and Glorie et al. (2022), Sm–Nd; e.g. Fisher et al. (2020)] isotopic systems. Apatite is more labile than zircon during physical and chemical weathering processes and is, therefore, more likely to represent first-cycle detritus, potentially including from more mafic sources than zircon (Chew and Spikings, 2021; Chew et al., 2011; Gillespie et al., 2018; Glorie et al., 2022). Hence, combinations of detrital zircon and apatite may, in some respects, complement each other, where zircon retains an encompassing (multi-cycle) history of felsic crust, whereas apatite provides a more restricted (first-cycle) view of crust, including more mafic components. However, interpreting apatite ages may not be so straightforward given its relatively low U–Pb closure temperature of ~375 to 600 °C compared to zircon (>900 °C) (Chew and Spikings, 2015). Therefore, the apatite U–Pb system is more susceptible to disturbance/recrystallisation post-magmatic crystallisation than zircon (Chew and Spikings, 2021; Kirkland et al., 2018; Schoene and Bowring, 2007).

This work reports time-constrained isotopic data from detrital zircon (U–Pb, Lu–Hf) and apatite (U–Pb, Lu–Hf, Sm–Nd), collected from ephemeral streams draining the East Pilbara Terrane. These results from detrital grains demonstrate continental-scale sediment dispersal across Western Australia and inform on the early construction and recycling of the Pilbara Craton. Using these data, we develop a model of dome unroofing, incorporating previous isotopic (Gardiner et al., 2017; Kemp et al., 2015; Kemp et al., 2023; Petersson et al., 2020; Petersson et al., 2019a; Salerno et al., 2021) and geological mapping (GSWA, 2023; Hickman, 1990; Van Kranendonk et al., 2007a; Wiemer et al., 2018), which may be applicable to some other Archean granite-greenstone terranes.

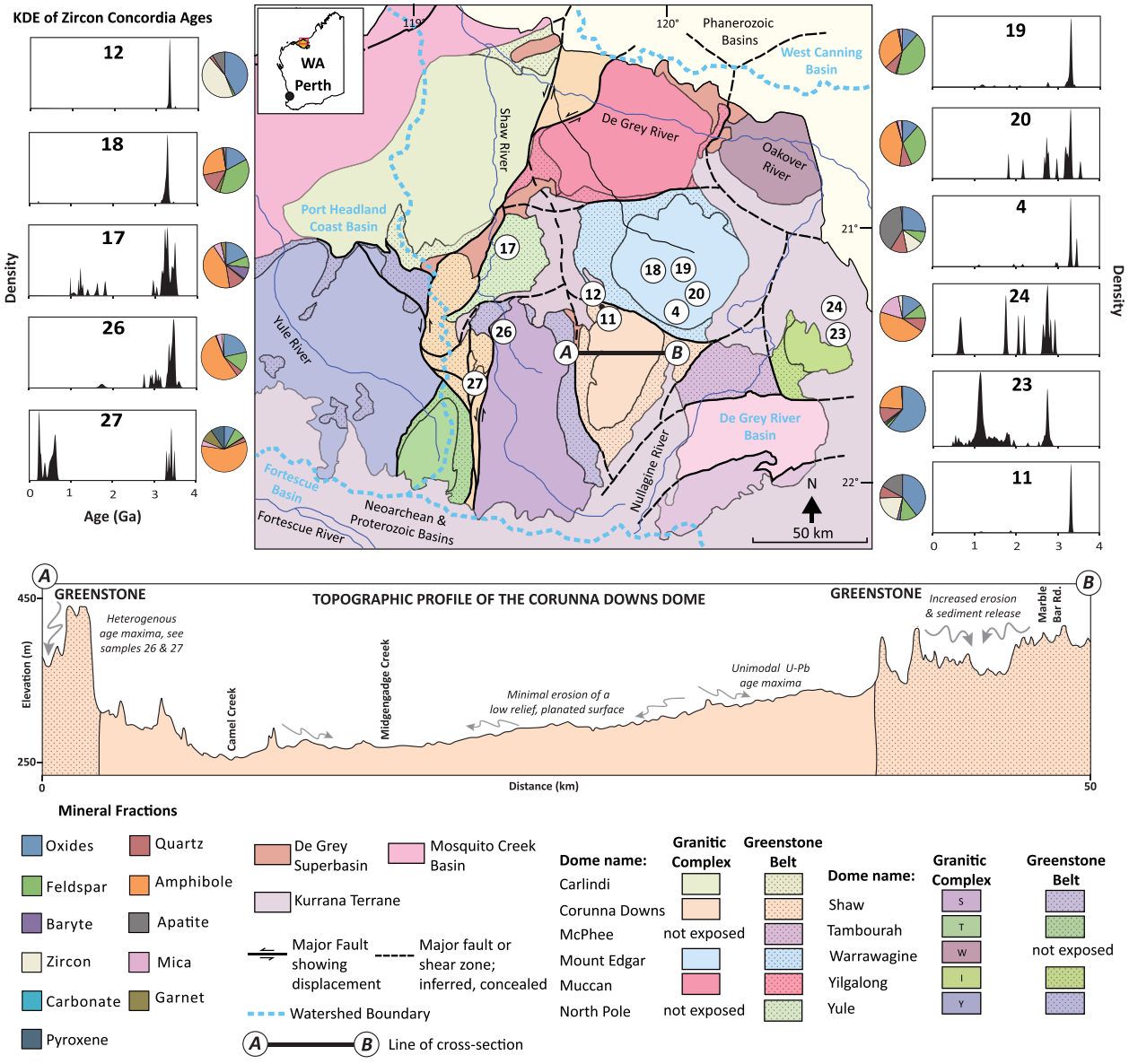

Fig. 1. Simplified geological map of the East Pilbara Terrane showing major drainage systems. To the sides are kernel density estimates of zircon concordia ages (filtering for >10 % discordance) and mineral fraction pie charts. Line A-B shows an illustrative topographic profile of the Corunna Downs Dome and surrounding greenstone belts; note the vertical exaggeration. The geodetic system used is WGS 84. Geological map of the East Pilbara Terrane adapted after Hickman (2021).

2. Geological background

The Pilbara Craton represents a rare occurrence of extensively exposed Paleo to Mesoarchean crust and offers important insights into early crustal evolution. Some workers infer that crust production within the Pilbara Craton began at c. 3.8 Ga as implied by ages of inherited zircon and Pb and Hf isotope systematics of Eoarchean gneisses (Gardiner et al., 2017; Hartnady and Kirkland, 2019; Petersson et al., 2019b). During the protracted (c. 3.8–3.0 Ga) construction of the Pilbara Craton, mafic lithologies may have dominated crust production globally (Dhuime et al., 2015).

Some workers have argued that this period encompasses the transition from an earlier, hotter, and more vertical tectonic regime to the more modern style of horizontal plate tectonics (Dhuime et al., 2012; Dhuime et al., 2015; Hartnady and Kirkland, 2019; Hawkesworth et al., 2020; Korenaga, 2013). Conversely, other workers maintain that subduction-type settings with mobile lid dynamics was operational from the Eoarchean (Nutman et al., 2021; Windley et al., 2021).

Unconformable Neoarchean and Proterozoic metasedimentary rock units overlie much (>80 %) of the Pilbara Craton, and only the northern (60,000 km^2) portion is exposed as an inlier (Hickman and Van Kranendonk, 2012). The exposed geology is classified into three tectonic components, the De Grey Superbasin (3.1–2.9 Ga), the West Pilbara Superterrane (3.3–3.1 Ga), and the East Pilbara Terrane (3.8–3.1 Ga) (Fig. 1) (Van Kranendonk et al., 2004).

The East Pilbara Terrane represents the classic example of a dome and basin granite-greenstone terrane (Hickman and Van Kranendonk, 2012; Jahn et al., 1981; Myers, 1993; Van Kranendonk et al., 2007b). The granitoid domes of the East Pilbara Terrane are composite intrusions formed from several generations of variably metamorphosed and deformed felsic igneous rocks (tonalite-trondhjemite-granodiorite — TTGs). The domes exhibit a spatial zonation from younger, less radiogenic (−ve εHf and εNd) cores to juvenile, more radiogenic (+ve εHf and εNd) rims (Gardiner et al., 2017). Greenstone belts bound the granitoid domes and exhibit lower amphibolite to greenschist and prehnite-pumpellyite facies metamorphism with increasing distance from domes (Bickle et al., 1985). Such greenstone successions predominantly comprise weakly metamorphosed ultramafic to mafic extrusive volcanic sequences intercalated with sedimentary package (Hickman, 1990; Myers, 1993; Petersson et al., 2020). The dome and basin terrane of the East Pilbara Terrane is interpreted to have formed from episodic granitoid intrusion, with associated deformation of the overlying greenstone within the mid to lower crust from c. 3.60–3.25 Ga (Hickman and Van Kranendonk, 2012; Sandiford et al., 2004; Van Kranendonk et al., 2004).

Ephemeral river systems of unconsolidated clay, silt, sand, gravel, and localised calcrete dominate the lowland drainage basins of the Pilbara Craton (Hocking et al., 2001). These recent sediments were used as the sampling medium in this study (Table 1; Fig. 1).

3. Methods

3.1. Location and sampling

Eleven 1–2 kg sand samples from ephemeral streams were collected across the East Pilbara Terrane, broadly centred around the Marble Bar town site (Table 1; Fig. 1). Tributaries of the Oakover, Fortescue, Shaw, and Nullagine rivers were sampled. For detailed location information, see Appendix 1.

3.2. Sample processing

The collected sands were concentrated for apatite and zircon via conventional heavy mineral processing steps at Curtin University. A riffle splitter was used to ensure subsequent concentrates were representative. For each sample, initial sieving at <425 μm yielded fractions of c. 500 g, which underwent heavy mineral separation via a Jasper Canyon Research shaking platform (Dumitru, 2016) and lithium heteropolytungstate heavy liquid (2.85 g/cm^3). A handheld neodymium magnet was first used to remove coarse ferric fragments. Following coarse fragment removal, three rounds of Frantz isodynamic magnetic separation using a constant side-slope angle of 10° but varying amperages (~0.4, 1 and 1.7 A) were implemented to retrieve three separates of varying magnetic susceptibility (Strong and Driscoll, 2016). The final non-magnetic fraction (>0.5 g) was then bulk-mounted into 25 mm diameter epoxy rounds.

Polishing (to a 1 μm finish) ensured that grains were sufficiently flat and exposed. Minerals were mapped using a TESCAN Integrated Mineral Analyser (TIMA). Additional imaging, including cathodoluminescence and backscatter electron, was undertaken using a Clara FE-SEM. The imaging process identified internal textures and crystal morphologies, aiding analysis positioning. Target apatite and zircon grains for isotopic analysis were chosen based on TIMA phase identification and SEM images.

Table 1
Summary table of sample localities, analyses performed and underlying geological unit. *Ages reported are zircon U-Pb weighted mean crystallisation dates of the crystalline basement (GSWA, 2023).

Sample ID	Latitude	Longitude	UTM	Analysis	Drainage	Unit	Age* (Ma)
4	−21.3504	120.0559	51 K 194,649 7,636,214	Zircon U–Pb, Lu–Hf	House Creek	Kennell Granodiorite	3315 ± 2
11	−21.3718	119.8159	50 K 792,017 7,634,084	Zircon U–Pb, Lu–Hf	Camel & Sandy Creeks	Apex Basalt	3459–3434
12	−21.3364	119.7898	50 K 789,372 7,638,051	Zircon U–Pb, Lu–Hf	Camel Creek	Euro Basalt	3350–3335
17	−21.0486	119.3918	50 K 748,550 7,670,608	Zircon U–Pb, Lu–Hf	Shaw River	Mount Ada Basalt	3470–3469
18	−21.1836	120.0225	51 K 190,824 7,654,631	Zircon U–Pb, Lu–Hf. Apatite U–Pb, Sm–Nd, Lu–Hf	Yondicoogina Creek	Fig Tree Gneiss	3448–3416
19	−21.1931	120.1282	51 K 201,835 7,653,786	Zircon U–Pb, Lu–Hf. Apatite U–Pb, Sm–Nd, Lu–Hf	Mount Creek	Bishop Creek Monzonite	3246–3223
20	−21.2112	120.262	51 K 215,768 7,652,024	Zircon U–Pb, Lu–Hf	Talga River	Bishop Creek Monzonite	3246–3223
23	−21.3213	120.8689	51 K 278,957 7,640,802	Zircon U–Pb, Lu–Hf	Garrigan Creek	Carawine Dolomite	2629–2565
26	−21.5304	119.3427	50 K 742,651 7,617,329	Zircon U–Pb, Lu–Hf. Apatite U–Pb, Sm–Nd, Lu–Hf	Mulgandinnah River	Callina Supersuite	3484–3462
27	−21.6203	119.1943	50 K 727,132 7,607,600	Zircon U–Pb	Mulgandinnah River	Euro Basalt	3350–3335

3.3. Zircon U–Pb and Lu–Hf

Four split-stream U–Pb/Lu–Hf sessions were undertaken at the GeoHistory Facility, JdLC, Curtin University. Zircon U–Pb data was collected using an Agilent 8900 ICP-MS, whereas Hf isotopes were collected contemporaneously via a Nu Plasma II MC-ICP-MS. Ablations used a RESOlution LE193 nm ArF laser and a Lauren Technic S155 cell. A relatively small spot of 38 μm was used for split-stream laser analyses, necessitated by the zircon grain size and internal complexity. For further analytical details, see Appendix 1.

Zircon downhole fractionation can vary with the zircon crystal state; hence, zircons with $^{207}Pb/^{206}Pb$ ages >2.4 Ga were reduced using OG1 as the primary reference, whereas <2.4 Ga zircon were reduced using GJ1, so the reference material best matched unknown ablation responses. For all sessions, the following (primary or secondary) reference materials were used: Plešovice 337.13 ± 0.37 Ma (Sláma et al., 2008), GJ1 601.95 ± 0.40 (Jackson et al., 2004), Maniitsoq 3008.70 ± 0.72 Ma (Marsh et al., 2019) and OG1 3465.4 ± 0.6 Ma (Stern et al., 2009). Secondary reference material yielded weighted mean ages within 2σ or 2SD uncertainty of the expected value when reduced using an appropriate primary reference material (Table 2) (Appendix 2).

For zircon Lu–Hf analyses, secondary reference materials included Plešovice $^{176}Hf/^{177}Hf$ 0.282482 ± 0.000013 (Sláma et al., 2008), R33 0.282764 ± 0.000014 (Fisher et al., 2014a), GJ1 0.282000 ± 0.000025 (Morel et al., 2008) and FC1 0.282184 ± 0.000016 (Woodhead and Hergt, 2005) and OG1 0.280633 ± 0.000034 (Coyner et al., 2004; Kemp et al., 2017). Secondary reference $^{176}Hf/^{177}Hf$ ratios (Table 3) (Appendix 3) and the stable isotope ratio $^{178}Hf/^{177}Hf$ were within 2σ error of reported values (Fisher et al., 2014b; Sláma et al., 2008). Fixed ratios of $^{176}Yb/^{173}Yb = 0.7962$ and $^{176}Lu/^{175}Lu = 0.02655$ were used to correct for isobaric interferences on ^{176}Hf (Chu et al., 2002; Hartnady et al., 2019). The contributions of ^{176}Yb and ^{176}Lu were then subtracted from the total ^{176} mass signal to obtain the interference-corrected $^{176}Hf/^{177}Hf$.

3.4. Apatite U–Pb

U–Pb analyses of apatite were undertaken using the LA–ICP–MS at the JdLC at Curtin University utilising a RESOlution 193 nm excimer laser ablation system connected to an Agilent 8900 ICP–MS with a RESOlution LE193 nm ArF and a Lauren Technic S155 cell ICP–MS. A 38 μm spot size, fluence of 2 J/cm^{2,} and a 5 Hz repetition were used. The primary reference material used for U–Pb analysis was Madagascar (MAD2) apatite (Thomson et al., 2012). Secondary reference materials included the Mt. McClure apatite (MMC) 523.51 ± 1.47 (Schoene and Bowring, 2006) and Duluth Complex (FC) apatite 1099.1 ± 0.2 Ma (Schmitz et al., 2003) (Appendix 2). Ages obtained from the secondary reference materials via anchored regressions are within 2σ uncertainty of the expected results (e.g. FC1, Duluth Complex 1079 ± 22, MSWD = 0.66; n = 19; Mt. McClure 522 ± 11, MSWD = 0.93; n = 14; see Appendix 2).

3.5. Apatite Sm–Nd and Lu–Hf

Sm–Nd and trace element geochemistry analyses of apatite were undertaken using the LA–ICP–MS at the JdLC at Curtin University. A RESOlution 193 nm excimer laser ablation system was connected to the Agilent 8900 ICP–MS with a RESOlution LE193 nm ArF and a Lauren Technic S155 cell ICP–MS. A 50 μm spot size, fluence of 2 J/cm^{2,} and a 5 Hz repetition were used. Sm–Nd data for apatite was collected during a single session. Durango apatite was the matrix-matched primary reference material for Sm–Nd and trace element analysis. Secondary standards included the Otter Lake apatite $^{143}Nd/^{144}Nd_i = 0.511447$ (Yang et al., 2014) along with the Durango Apatite $^{143}Nd/^{144}Nd_i = 0.512472$ (Yang et al., 2014), reduced against Otter Lake. All analyses fell within the 2SD uncertainty of previously reported values (Appendix 4). Durango apatite yielded a mean $^{143}Nd/^{144}Nd$ initial ratio of 0.512483 ± 0.000094 2SD and Otter Lake 0.511452 ± 0.000043 2SD (Appendix 4).

Table 2
Summary table of U–Pb zircon secondary reference material. * $^{207}Pb/^{206}Pb$ ages for zircons OG1 and Maniitsoq whereas $^{206}Pb/^{238}U$ ages are reported for all other reference material.

Session 1

Reference	Primary Reference	Reported Age (Ma)	2σ	Age Ma* (Weighted Mean 95 % confidence)	2SD	2σ	MSWD	p	n
Plešovice	GJ1	337.13 (Sláma et al., 2008)	0.37	332	8	4	0.52	0.96	22
GJ1	Plesovice	601.95 (Jackson et al., 2004)	0.40	596	12	6	0.42	1.00	37
OG1	Maniitsoq	3465.4 (Stern et al., 2009)	0.60	3465	11	3	1.40	0.07	33
Maniitsoq	OG1	3008.7 (Marsh et al., 2019)	0.72	3005	8	5	0.68	0.76	12

Session 2

Reference	Primary Reference	Reported Age (Ma)	2σ	Age Ma* (Weighted Mean 95 % confidence)	2SD	2σ	MSWD	p	n
Plešovice	GJ1	337.13 (Sláma et al., 2008)	0.37	334	3	1	1.20	0.28	8
GJ1	Plešovice	601.95 (Jackson et al., 2004)	0.40	606	3	3	0.50	0.88	11
OG1	Maniitsoq	3465.4 (Stern et al., 2009)	0.60	3466	7	3	1.00	0.43	17
Maniitsoq	OG1	3008.7 (Marsh et al., 2019)	0.72	3014	14	6	1.40	0.15	12

Session 3

Reference	Primary Reference	Reported Age (Ma)	2σ	Age Ma* (Weighted Mean 95 % confidence)	2SD	2σ	MSWD	p	n
Plešovice	GJ1	337.13 (Sláma et al., 2008)	0.37	341	4	2	1.20	0.26	10
GJ1	Plešovice	601.95 (Jackson et al., 2004)	0.40	596	4	5	0.19	1.00	14
OG1	Maniitsoq	3465.4 (Stern et al., 2009)	0.60	3465	5	5	0.40	0.95	11
Maniitsoq	OG1	3008.7 (Marsh et al., 2019)	0.72	3008	6	4	0.50	1.00	16

Session 4

Reference	Primary Reference	Reported Age (Ma)	2σ	Age Ma* (Weighted Mean 95 % confidence)	2SD	2σ	MSWD	p	n
Plešovice	GJ1	337.13 (Sláma et al., 2008)	0.37	339	4	2	2.10	0.02	12
GJ1	Plešovice	601.95 (Jackson et al., 2004)	0.40	599	6	4	0.66	0.84	18
OG1	Maniitsoq	3465.4 (Stern et al., 2009)	0.60	3467	8	4	0.88	0.57	14
Maniitsoq	OG1	3008.7 (Marsh et al., 2019)	0.72	3004	6	4	1.20	0.29	17

Table 3
Summary table of Hf results for zircon secondary reference material.

Session 1									
Reference	Primary Reference	Expected $^{176}Hf/^{177}Hf$	2SD	$^{176}Hf/^{177}Hf$ (Weighted Mean 95 % confidence)	2σ	MSWD	$^{176}Hf/^{177}Hf$ (Arithmetic Mean)	2SD	*n*
Plešovice	Mudtank	0.282482 (Sláma et al., 2008)	0.000013	0.282494	0.000022	1.1	0.282491	0.000078	12
R33	Mudtank	0.282764 (Fisher et al., 2014)	0.000014	0.282770	0.000017	1.2	0.282769	0.000083	20
GJ1	Mudtank	0.282000 (Morel et al., 2008)	0.000025	0.282012	0.000027	1.7	0.282013	0.000116	20
OG1	Mudtank	0.280633 (Kemp et al., 2017)	0.000034	0.280664	0.000018	0.9	0.280665	0.000073	19
Session 2									
Reference	**Primary Reference**	**Expected $^{176}Hf/^{177}Hf$**	**2SD**	**$^{176}Hf/^{177}Hf$ (Weighted Mean 95 % confidence)**	**2σ**	**MSWD**	**$^{176}Hf/^{177}Hf$ (Arithmetic Mean)**	**2SD**	***n***
Plešovice	Mudtank	0.282482 (Sláma et al., 2008)	0.000013	0.282487	0.00002	0.5	0.282488	0.000045	12
R33	Mudtank	0.282764 (Fisher et al., 2014)	0.000014	0.282761	0.000017	0.7	0.282762	0.000053	15
GJ1	Mudtank	0.282000 (Morel et al., 2008)	0.000025	0.282018	0.000021	1.0	0.280019	0.000082	16
Maniitsoq	Mudtank	0.280862 (Marsh et al., 2019)	0.000021	0.280889	0.000018	0.5	0.280887	0.000047	16
Session 3									
Reference	**Primary Reference**	**Expected $^{176}Hf/^{177}Hf$**	**2SD**	**$^{176}Hf/^{177}Hf$ (Weighted Mean 95 % confidence)**	**2σ**	**MSWD**	**$^{176}Hf/^{177}Hf$ (Arithmetic Mean)**	**2SD**	***n***
Plešovice	GJ1	0.282482 (Sláma et al., 2008)	0.000013	0.282463	0.000022	0.3	0.282463	0.000042	12
R33	GJ1	0.282764 (Fisher et al., 2014)	0.000014	0.282754	0.000016	0.6	0.282752	0.000048	16
FC1	GJ1	0.282184 (Woodhead and Hergt, 2005)	0.000012	0.282177	0.000022	0.7	0.282180	0.000070	12
OG1	GJ1	0.280633 (Kemp et al., 2017)	0.000034	0.280594	0.000018	0.9	0.280596	0.000071	18
Session 4									
Reference	**Primary Reference**	**Expected $^{176}Hf/^{177}Hf$**	**2SD**	**$^{176}Hf/^{177}Hf$ (Weighted Mean 95 % confidence)**	**2σ**	**MSWD**	**$^{176}Hf/^{177}Hf$ (Arithmetic Mean)**	**2SD**	***n***
Plešovice	GJ1	0.282482 (Sláma et al., 2008)	0.000013	0.282461	0.000023	1.0	0.282466	0.000077	12
R33	GJ1	0.282764 (Fisher et al., 2014)	0.000014	0.282756	0.000016	0.9	0.282754	0.000060	17
FC1	GJ1	0.282184 (Woodhead and Hergt, 2005)	0.000012	0.282204	0.000024	1.2	0.282205	0.000080	10
OG1	GJ1	0.280633 (Kemp et al., 2017)	0.000034	0.280637	0.000021	1.0	0.280626	0.000080	17

Analyses of apatite Lu–Hf isotopes were performed at the University of Adelaide. Due to the isobaric interference of ^{176}Lu and ^{176}Yb on ^{176}Hf, dissolution and chemical separation are conventionally required for high Lu–Hf phases prior to mass spectrometry, resulting in the loss of spatial context for isotopic information and necessitating time consuming wet-chemical separation. However, the Simpson et al. (2021) approach allows for in situ Lu–Hf isotopic analysis using laser ablation. A RESOlution 193 nm excimer laser ablation system coupled to an Agilent 8900 ICP–MS/MS was used with analytical conditions identical to those in Glorie et al. (2022). In-house reference apatite Bamble with a corrected Lu–Hf age of 1097 ± 5 Ma (Simpson et al., 2021) was monitored as an accuracy check and is consistent with previously published data (Glorie et al., 2022). The resulting apatite Lu–Hf ages were calculated both as inverse isochron (Li and Vermeesch, 2021) intercept ages as well as common Hf-corrected weighted mean ages (excluding data with $^{177}Hf/^{176}Hf$ ratios >2). For more details, see Appendix 4.

4. Results

4.1. Zircon

Zircon concordia ages are interpreted as the ages of zircon-crystallising rocks within the detrital source region(s) or as the ages of detrital components within sediments that have been reworked into ephemeral stream sediment (Fig. 2). The samples covered a large geographic area (Fig. 1) and, therefore, may represent a variety of Pilbara lithologies and potentially distal non-Pilbara sources.

Some samples yield large percentages of discordant zircon U–Pb analyses. For example, of the 116 U–Pb analyses undertaken on Sample 26, 77 % are >10 % discordant (Appendix 2). However, the basement geology underlying the stream sediment samples appears to have little control over the degree to which the detrital grains have lost radiogenic Pb (Appendix 2). Instead, a combination of factors appear to have acted in unison to yield discordant grains; namely, the antiquity of many grains means they would have accumulated variable radiation damage,

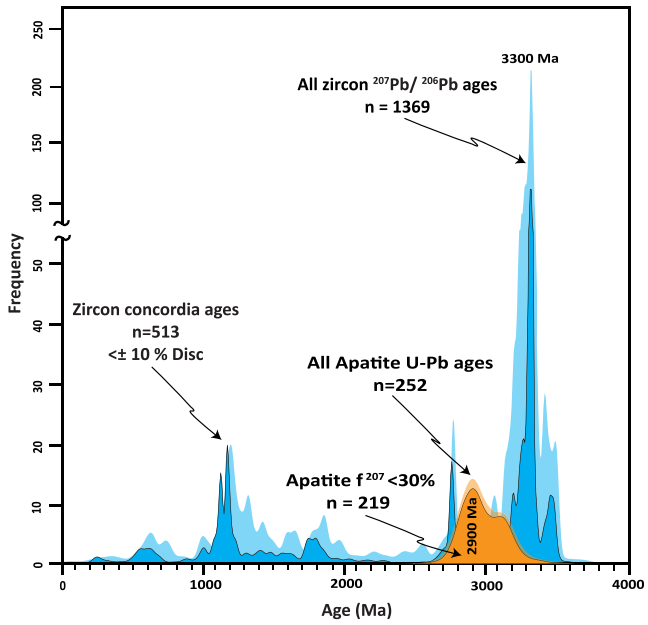

Fig. 2. Stacked adaptive kernel density estimates for ages obtained from detrital apatite and zircon. The light orange KDE represents all ^{207}Pb corrected U-Pb apatite ages, whilst the solid orange KDE is filtered for <30 % f^{207}. The light blue KDE is unfiltered $^{207}Pb/^{206}Pb$ zircon ages, and the solid blue KDE represents zircon concordia ages within ± 10 % of concordance. Note the scale break in the Y-axis.

dependent on age, U, and Th content, and access to fluids (Fig. 2) (Appendix 2). The prolonged subaerial exposure would have facilitated access to hydrothermal/meteoric fluids that would have stripped Pb in susceptible grains with fluid pathways (Pidgeon et al., 2017). Additionally, as demonstrated for Archean zircon grains, prolonged exposure to low-temperature environments would have inhibited structural recovery in any damaged zircon grains (Herrmann et al., 2021; Pidgeon et al., 2017). Moreover, we adopted a bulk mounting and random spot-picking strategy to minimise zircon selection bias during LA–ICP–MS analysis (Dröllner et al., 2021); it could be reasonably expected to incorporate more discordant analyses, more representative of actual zircon load. Concordia ages provide optimum use of the U–Pb and Pb–Pb systems and, importantly, give an objective measure of concordance, with data being filtered for greater than ±10 % discordance. A compilation of zircon concordia diagrams for all samples is given in Appendix 2. The zircon grains separated from the sand samples represent a diverse population of crystal morphologies and were therefore categorised based on age. The youngest concordant zircon grain is 221 Ma, whilst the oldest is 3586 Ma (Fig. 2).

4.1.1. 2.6–3.6 Ga zircons

Over 70 % of zircon grains are between 3.6 and 2.6 Ga. Zircon grains of this category are generally well-rounded (with aspect ratios of c. 1:1), transparent to opaque brown, anhedral, equant and small, with typical lengths of only up to 40 µm (Fig. 3). Sector zoning is the dominant texture but is often truncated at grain margins. The surface pitting and the highly rounded nature of these grains indicate high degrees of mechanical abrasion during sedimentary reworking. 3.6–2.6 Ga zircon grains largely constitute samples with simple unimodal age populations (Fig. 1); such age distributions suggest direct derivation from the underlying crystalline basement.

4.1.2. 2.6–1.2 Ga zircons

Twelve per cent of concordant analyses are in this age group. These grains are primarily euhedral to sub-euhedral, opaque light brown to cloudy transparent, with variable lengths of 50–120 µm (Fig. 3). Most of these zircons have simple concentric zoning, often truncated at grain margins. Grains of this category show less physical damage than older zircons, with larger and better-preserved prismatic crystal shapes with aspect ratios generally of 2:1. Rare apatite inclusions form small (<10 µm) anhedral grains within the cores of concentrically zoned >40 µm zircon crystals.

4.1.3. < 1.2 Ga zircons

Twenty-five per cent of zircons ages are younger than 1.2 Ga. In this age group, zircon grains are predominantly euhedral, showing tabular to prismatic crystals with minor abrasion compared to older grains. Sharp concentric oscillatory zoning is common, and grain lengths are generally over 50 µm (Fig. 3). These zircon grains are generally transparent to opaque light brown, with aspect ratios exceeding 3:1.

4.2. Apatite

4.2.1. Apatite morphology

Apatites typically occur as anhedral to sub-euhedral rounded grains with crystals generally exceeding 100 µm in length. Apatite is opaque pale brown to transparent, usually homogenous with no pronounced zoning; however, faint magmatic zoning is apparent in some of the largest (>100 µm) grains (Fig. 3).

4.2.2. Apatite geochronology

Apatite can host significant concentrations of common lead (Pb_c), and U–Pb data typically sit along two (or more) Pb mixing lines that generally stretch between a time-significant radiogenic and initial Pb_c component(s). On a Tera-Wasserburg plot, such data generally reveal lower intercepts representing the timing of radiogenic Pb accumulation. A ^{207}Pb correction (Compston, 1999) can be performed using an initial Pb_c composition first estimated from the apparent U/Pb age and an appropriate Pb model (Stacey and Kramers, 1975). This initial ^{207}Pb corrected age can then be used to recalculate an apparent $^{207}Pb/^{206}Pb_i$, and the procedure iterated until no subsequent change in corrected age occurs. This method converges towards a mean $^{207}Pb/^{206}Pb_i$ of 1.10 for the detrital apatite population. To verify the results of this approach, we also calculated internal, individual apatite isochrons, where up to six analyses on the same crystal were performed. This technique yielded $^{207}Pb/^{206}Pb_i$ upper intercepts of 1.10 ± 0.20, consistent with the Stacey and Kramers (1975) terrestrial Pb model for c. 3.0 Ga crust. Additional information regarding the common Pb correction is provided in Appendix 2. The detrital apatite U–Pb ages are more temporally restricted than the zircon ages, with apatite ^{207}Pb corrected ages implying a near unimodal population at c. 2.9 Ga (Fig. 2) (Fig. 4).

A total of 261 Sm–Nd apatite analyses were undertaken on samples 18, 19, and 26. All analyses yield a 3157 ± 66 Ma isochron with an initial $^{143}Nd/^{144}Nd$ of 0.508504 ± 0.000084 (MSWD = 2.3) (Fig. 5) (Appendix 4). A further 83 apatite Lu–Hf analyses were also undertaken on samples 18, 19, and 23, which yielded a 3181 ± 33 Ma isochron, with an initial $^{177}Hf/^{176}Hf$ of 3.566 ± 0.037 (MSWD = 1.2) (Fig. 5) (Appendix 4).

5. Discussion

5.1. Sediment transport

5.1.1. Pilbara provenance

The detrital zircon ages offer a broad snapshot of Paleoarchean to early Triassic magmatism throughout Western Australia (Fig. 2). The oldest zircon age component (3.6–2.6 Ga) comprises 70 % of zircon analyses and is predominantly made up of highly rounded, small (≤50 µm) grains consistent with a multi-cycle history of reworking from the crystalline basement of the Pilbara Craton (Fig. 3). Extensive basement zircon U–Pb geochronology has shown that magmatism in the Pilbara Craton occurred in major episodes, each contributing to the

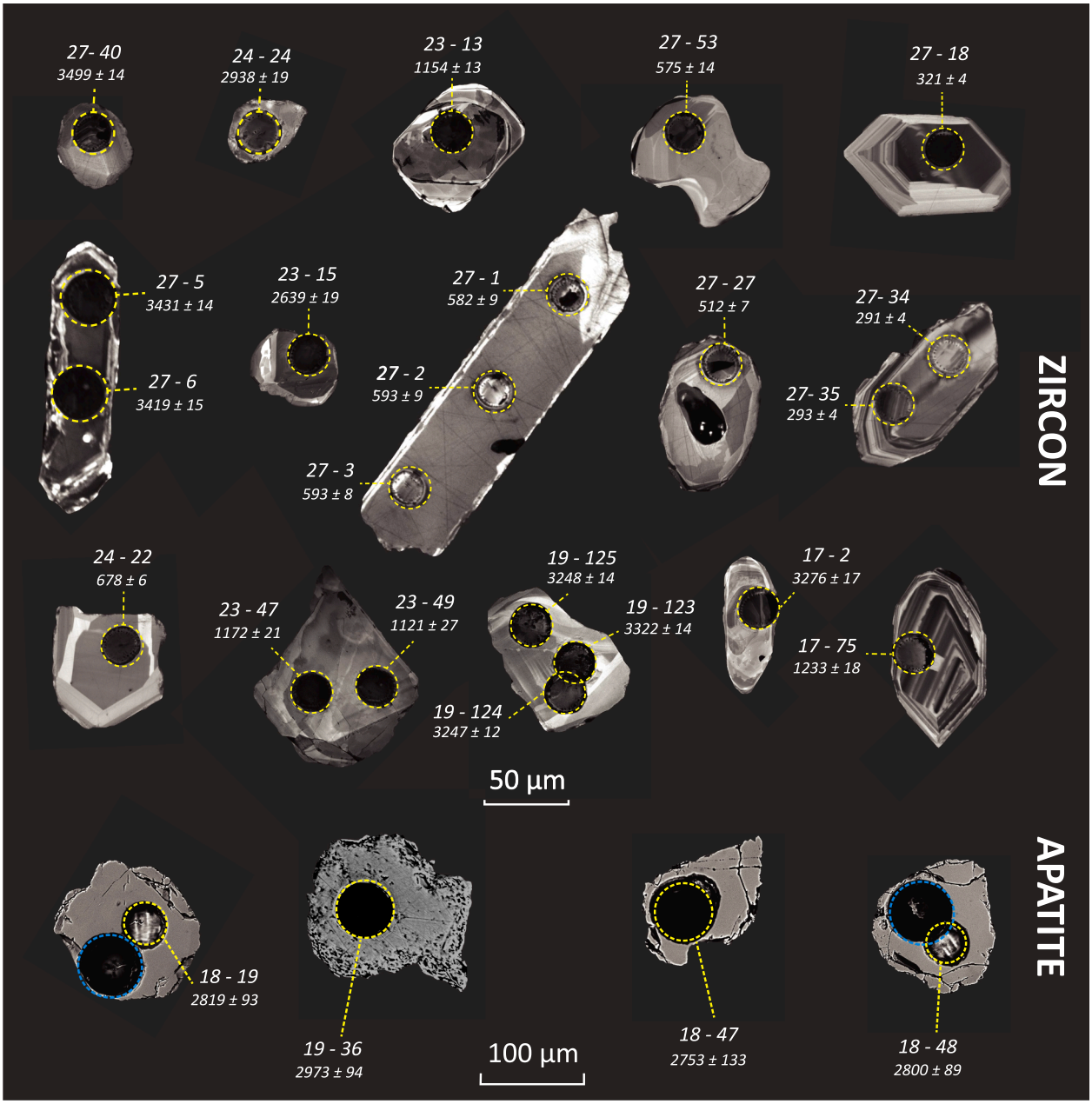

Fig. 3. Top rows: Cathodoluminescence images of representative zircon grains showing sample and spot number, laser spot location (38 µm) and concordia age (Ma ± 2σ). Only grains ≤ 10 % discordant are shown. Bottom row: A compilation of backscatter electron images of representative apatite. The smaller spot is a 38 µm U-Pb ablation, whereas the larger spot is a 50 µm ablation.

formation of the granitoid domes (Hickman and Van Kranendonk, 2012; Nelson, 2005). The Archean detrital zircon reflects the timing of this magmatism, with distinct age peaks at 3.45, 3.30, 3.14, and 2.95 Ga defined by 38, 80, 136, and 11 grains, respectively. The c. 3.45 Ga zircon grains are likely derived from the Callina Supersuite, a voluminous intrusion of TTG magmas that partially occurs as a sheeted dyke complex in the North Shaw Suite (Van Kranendonk, 2008). The emplacement of the Callina Supersuite led to localised crustal thickening, which commenced the intrusion of granitoid domes (Hickman and Van Kranendonk, 2012). The Cleland and Emu Pool Supersuite have contributed to the most significant age peak at c. 3.30 Ga, and both suites predominantly comprise the Mount Edgar dome (GSWA, 2023; Roberts and Tikoff, 2021) (Fig. 1). The c. 2.9–2.8 Ga zircon population is consistent with a Cutinduna and Split Rock Supersuite source. Both magmatic supersuites occur in the west to northwestern portion of the EPT and consist of granitoids emplaced during the Mosquito Creek Orogeny (Fig. 1) (Hickman and Van Kranendonk, 2012).

The zircon U–Pb age populations have a pronounced geographical influence, with ephemeral stream sediment samples collected atop granitoid domes predominantly recording discrete, unimodal age components (Fig. 1). The felsic granitoid domes have a higher intrinsic zircon load than surrounding greenstones, thus dominating age components with their locally derived magmatic zircon. For instance, the Mt. Edgar dome was assembled over 3.46–2.83 Ga (Van Kranendonk et al., 2004) and samples 18, 19, 20 and 4 were collected from streams atop the dome (Table 1) (Fig. 1). Of the concordant ages obtained from those samples, 89 % fall within the dome-forming period. Conversely, samples collected from greenstones show a more heterogenous zircon U–Pb age distribution (Fig. 1), reflecting input from sources outside the Pilbara Craton, likely compounded by a lack of intrinsic zircon load from the

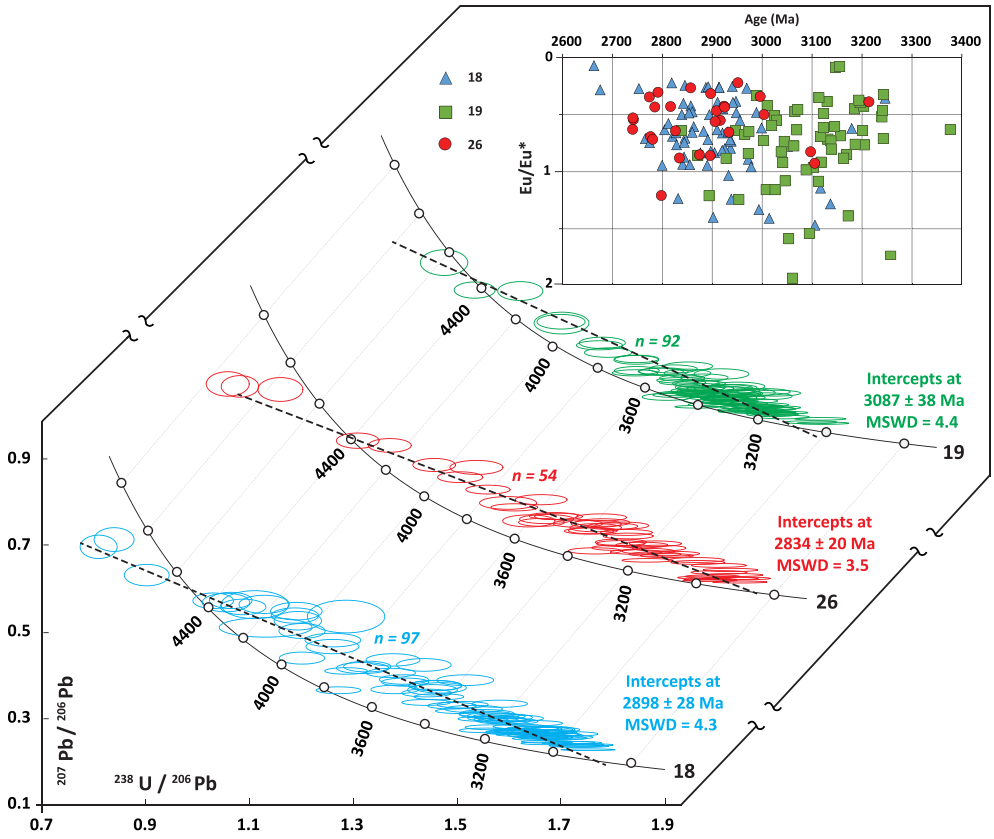

Fig. 4. Stacked Tera-Wasserburg concordia diagrams for apatite U-Pb analyses. Error ellipses and intercept uncertainties are shown at 2σ. A best fit Model-1 regression from Isoplot R (Vermeesch, 2018). Analyses with $^{238}U/^{206}Pb < 0.7$ are not presented graphically but are included in regression calculations. The inset plot shows apatite Eu/Eu* anomalies against f^{207} corrected ages (<30 %).

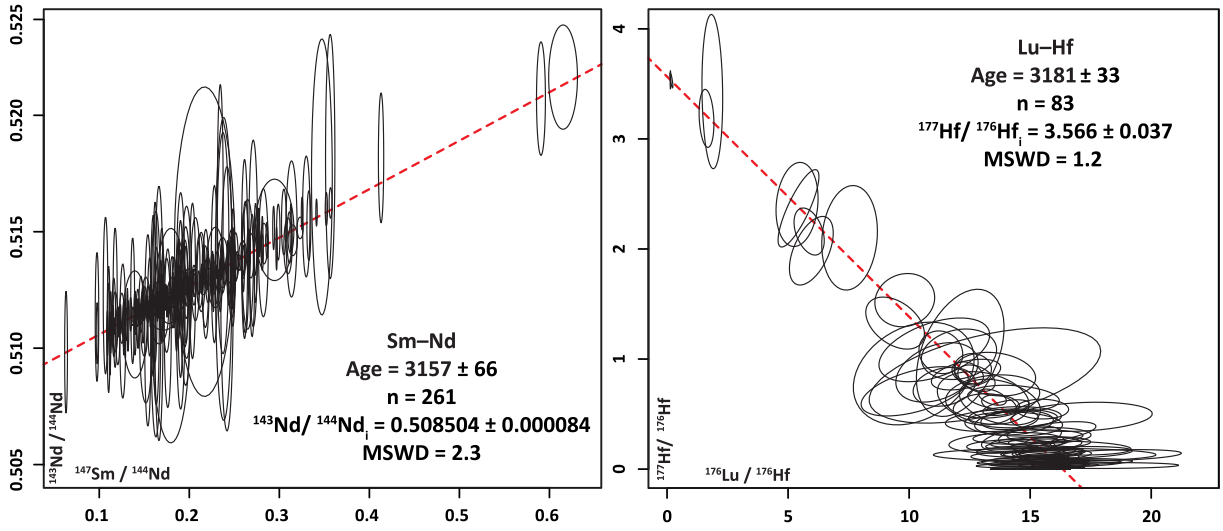

Fig. 5. Top: apatite Sm–Nd isochron for all apatite samples using the maximum likelihood model (Vermeesch, 2018). Bottom: Inverse apatite Lu–Hf isochron for apatite using the maximum likelihood of fit. All uncertainty ellipses are reported at 2σ.

predominantly mafic (zircon-poor) geology (Hickman, 2021; Myers, 1993; Van Kranendonk et al., 2007a).

Another control on the detrital load of contemporaneous sediment is the present-day physiography of the East Pilbara Terrane. The flat, low-lying granitoid domes are bound by supracrustal greenstone belts and sedimentary successions, forming areas of comparatively high topographic relief (Fig. 1) (Hickman and Van Kranendonk, 2012). Steep, unvegetated hills have increased erosion rates and thus, sediment release would be elevated from greenstone successions and overlaying regolith (Riebe et al., 2015). Coupled with the concept of intrinsic zircon load, the erosion of greenstones would rapidly release a diverse cargo of zircon grains into stream sediment. Conversely, the stream sediment of granitoid domes represents the product of slow, *in-situ* erosion of expansive outcrops of homogenous (unimodal age maxima) granitoid (Fig. 1).

5.1.2. Zircon from outside the Pilbara Craton

Thirty per cent of concordant zircon grains in this work are younger than 2.6 Ga and represent detritus ultimately derived from crystalline sources outside the Pilbara Craton. Given the localised catchment areas and the ephemeral nature of the streams sampled, they are unlikely to be the mechanism by which exotic zircons have been delivered to the Pilbara. Kinny et al. (2022) reported zircon U–Pb geochronology from ephemeral streams draining the metasediments at Jack Hills and found a suite of Neoarchean and younger grains. In both that study and this work, the distance to Proterozoic or younger lithologies and the widespread distribution of <2.6 Ga zircon within streams (e.g., samples 23 and 27 are 170 km apart, overlay Archean geology, yet both contain Palaeozoic zircon) are consistent with Mesozoic continental scale sediment movement systems (Craddock et al., 2019; Morón et al., 2019).

There is a general paucity of zircon ages between 2.6 and 2.0 Ga, consistent with a general lack of large-scale magmatism identified in WA during this period (GSWA, 2023). Discerning the provenance of <2.6 Ga zircon grains remains somewhat speculative based on age signature alone due to several potential sources having overlapping crystallisation ages (e.g., Albany-Fraser Orogen (AFO), Musgrave Province, Rudall Province, Capricorn Orogen). Zircon Lu–Hf signatures allow the refinement of such provenance interpretations. At c. 1.8 Ga, zircon εHf data ranges from −12 to +5 and is broadly sub-chondritic, much like signatures from the Capricorn Orogen, Halls Creek Orogen, the Biranup Zone or Rudall Province (Fig. 6). These magmatic complexes girdling the Yilgarn Craton likely supplied the Paleoproterozoic zircon grains to the Pilbara sediments. Additional detrital input was perhaps derived from granitoid plutons in the Northern Yilgarn craton and the Capricorn Orogen, Ashburton Basin, and Glenburgh Terrane, which are associated with c. 1750 Ma magmas and εHf signatures of −12 to +3.3 (Fig. 6) (Jahn et al., 2021).

The Rudall Province, on the eastern margin of the Pilbara Craton, is characterised by several episodes of Paleoproterozoic felsic magmatism with sub-chondritic εHf signatures, consistent with the prolonged reworking of an Archean Pilbara basement (Gardiner et al., 2018). Supracrustal material within the province is intruded by three generations of granitoid plutons (1. Kalkan Supersuite 1804–1762 Ma, 2. Krackatinny Supersuite 1589–1549 Ma and 3. Camel Suite 1310–1286 Ma) (Gardiner et al., 2018; GSWA, 2023). Some Pilbara stream detrital zircon εHf data (see samples 23 and 24) reveal a broadly sub-chondritic signature consistent with a Rudall Province source (Fig. 6).

Detrital age components at 1.3 Ga and 1.2 Ga (Fig. 2) may correspond to felsic magmatism during Stages 1 and 2 of the AFO (Fig. 6) (Spaggiari et al., 2014). However, εHf values between +2 and +10 are more radiogenic than typical AFO magmas and are, therefore, better correlated with the juvenile magmas of similar age and closer proximity in the Musgrave Province (Fig. 6) (Kirkland et al., 2013b).

The aforementioned source regions imply an extensive mechanism to transport detritus from the south while minimising damage to zircon grains (Fig. 3). During the late Palaeozoic, the Pilbara Craton, as part of the West Australian Craton, was a component of the Gondwana supercontinent and was situated north of Antarctica (Wopfner and Jin, 2009). Prior to the breakup of Gondwana, continental ice sheets flowing from the paleo-south pole carried and deposited an extensive covering of Permian to Carboniferous sediment (Morón et al., 2019). The ice sheets presumably contained a cargo of zircon collected from lithologies en route to the Pilbara Craton, which were ultimately deposited in Phanerozoic basins bounding the Pilbara Craton (Craddock et al., 2019). Within the post-glacial period, continental-scale fluvial systems originating from the south of East Gondwana continued transporting detritus (Morón et al., 2019). The detrital zircons from such fluvial systems within the Officer, Canning, Northern Carnarvon, and Roebuck Basin have age spectra that show a close similarity to those obtained from the East Pilbara Terrane (Fig. 2) (Haines et al., 2013; Morón et al., 2019; Zutterkirch et al., 2021). We conclude that the Palaeozoic paleocontinental configuration of Gondwana enabled the delivery of well-preserved zircon grains into the Pilbara Craton.

The youngest zircon population at c. 200–300 Ma is enigmatic, postdating the Gondwana sedimentation episode, and likely represents exotic material, given that no igneous rocks of this age range crop out in the Pilbara Craton or the West Australian Craton more generally. Zircon grains within this component have a distinct morphology, being larger (≥150 μm), euhedral with high aspect ratios exceeding 3.0, consistent with minimal abrasion during their transport (Fig. 3).

The Lhasa Terrane, an east–west trending tectonic belt in the Tibetan Plateau, represents a plausible provenance for young zircons. From the early Triassic onwards, southwards subduction beneath the Lhasa Terrane formed a backarc basin with felsic magmatism (Zhu et al., 2011a). During the early Jurassic break up of Gondwana, the Lhasa Terrane is believed to have rifted away from northwest Australia and collided with the Qiangtang terrane during the Himalayan orogeny (Zhu

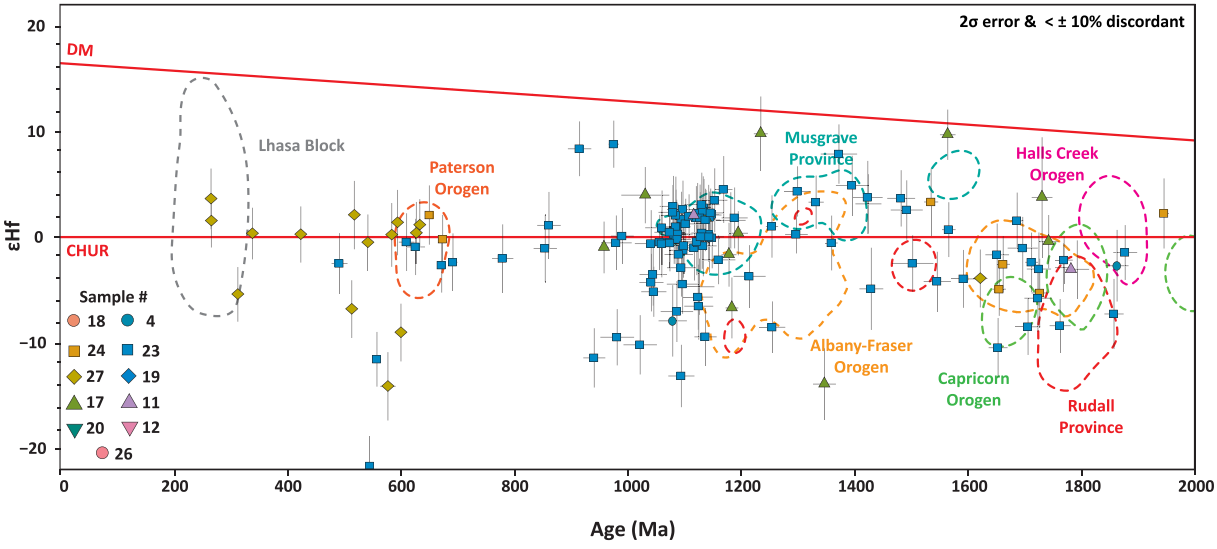

Fig. 6. εHf versus concordia age for Proterozoic and Phanerozoic detrital zircon from this study compared to crystalline basement samples compiled from previous work. Dashed areas represent 75 % peak density using fixed KDE bandwidth of εHf = 1.5 and age = 25 Ma. Data compiled from Gardiner et al. (2018); Johnson et al. (2017); Kirkland et al. (2013a); Kirkland et al. (2013b); Martin et al. (2017); Tucker et al. (2018).

et al., 2011a). Using detrital zircon ages and Hf isotope data, Zhu et al. (2011b) invoked a shared paleo-drainage system whereby detritus flowed between the sub-aerially exposed Lhasa Terrane and the Western Australia Craton. Detrital U–Pb zircon ages of c. 200–300 Ma and positive εHf signatures of −5.0 to +16.2 are reported for the Lhasa Terrane, tentatively correlating to those recorded in Fig. 6. (Zhu et al., 2011a; Zhu et al., 2011b). Furthermore, detrital zircon studies within the North West Shelf oil field off the coast of the Pilbara Craton area have reported Mesozoic zircon grains (Lewis and Sircombe, 2013; Morón et al., 2019; Zutterkirch et al., 2021).

Surficial deposits of the East Pilbara Terrane consist of isolated Cenozoic successions of iron-rich alluvial duricrust and pisolite (Hocking et al., 2001). These diverse but often fragmentary layers occur throughout the West Australian Craton (Hocking et al., 2001) and represent the remnants of a once extensive northwards-flowing Mesozoic fluvial system (Morón et al., 2019). Despite a period of stability and restricted sediment input following the breakup of Gondwana, exotic detrital zircons are abundant within the ephemeral streams sampled (Fig. 1). U–Pb zircon datasets for this unconsolidated cover in Western Australia support the widespread distribution of Proterozoic detritus atop the Archean basement (Hocking et al., 2001; Kinny et al., 2022; Veevers et al., 2005). Salama et al. (2022) reported a well-preserved population of c. 1000–2000 Ma zircon grains from regolith in the Yamarna Terrane, Eastern Yilgarn. Veevers et al. (2005) also demonstrated that various contemporaneous sands and regoliths along the southern margin of the Yilgarn Craton contain a cargo of zircon consistent with sources from the Pinjarra and Albany-Fraser Orogens. Large detrital loads of similarly Proterozoic-aged zircon grains are found across the northern margin of the Pilbara Craton (Dröllner et al., 2023; Zutterkirch et al., 2021). Hence, we posit that the Cenozoic strata of the Pilbara holds a reserve of far-transported Proterozoic zircon, which was periodically eroded, releasing grains into contemporary sediment.

5.1.3. *Apatite provenance and thermal history*

A diverse range of apatite U–Pb closure temperatures have been reported from laboratory and empirical studies (Chew and Spikings, 2021; Cochrane et al., 2014; Kirkland et al., 2018), with natural apatite likely closing to Pb diffusion over a temperature range of ~375 to 600 °C (Chew and Spikings, 2015). Grain size and fast diffusion pathways, such as fractures within apatite, highly influence specific closure temperatures. In addition, the U–Pb system of apatite is vulnerable to thermal disturbance and recrystallisation following initial formation (Chew and Spikings, 2021; Chew et al., 2011; Kirkland et al., 2018).

The closure temperature for Sm–Nd diffusion in apatite has been inferred to be as high as c. 950 °C (Cherniak, 2000) and the Lu–Hf system in apatite has a likely closure temperature of ~675–750 °C (Barfod et al., 2005; Glorie et al., 2022). Both isotope systems are, therefore, seemingly less susceptible to thermal resetting than the U–Pb system (Gillespie et al., 2022). The apatite Sm–Nd isochron (n = 261) age of 3157 ± 66 Ma. The inverse Lu–Hf isochron for apatite (n = 83) yielded an age of 3181 ± 33 Ma (MSWD = 1.2) (Fig. 5), which is strikingly similar to the Sm–Nd isochron. The matching isochrons for these different systems support an interpretation of a c. 3.2 Ga crystallisation age for an essentially unimodal apatite primary age component (Fig. 7).

By surface area, the Bishop Creek Monzonite is the largest constituent component of the Mt. Edgar Dome and has a crystallisation age of c. 3.24 Ga (GSWA, 2023). However, the assembly of the Mt. Edgar Dome was a protracted process and occurred over c. 3.4–2.8 (GSWA, 2023; Roberts and Tikoff, 2021). Further, the constituent supersuites of the Mt. Edgar Dome are variable in granitic composition from TTG to monzogranite (Bickle et al., 1985; Gardiner et al., 2017). Given its labile nature, apatite is unlikely to survive multiple reworking cycles (O'Sullivan et al., 2020) and, on average, can represent a more proximal detrital source than zircon. Samples 18 and 19 yielded 76 % of apatite U–Pb analyses, and both were collected from stream sediment atop the Bishop Creek Monzonite. Accordingly, the supersuites of the Mt. Edgar Dome likely represent the predominant source of detrital apatite analysed, representing the unimodal age signature from a restricted source seen in the Sm–Nd and Lu–Hf isochrons (Fig. 2) (Fig. 4).

There is a difference between the apatite ages obtained by the U–Pb and Sm–Nd/Lu–Hf isotopic systems (Fig. 7). Previous work has demonstrated that apatite U–Pb ages may record thermotectonic events at lower temperatures than magmatic crystallisation, such as cooling at mid-to-shallow crustal levels (Chew and Spikings, 2021). Alternatively, apatite U–Pb ages can represent prograde metamorphic processes within the U–Pb closure temperature range, thus resetting or recrystallising a primary age to a metamorphic age (Chew and Spikings, 2021; Kirkland et al., 2018).

The Moolyella monzogranite is part of the Split Rock Supersuite and forms a series of irregular stock-like outcrops between the Nullagine and

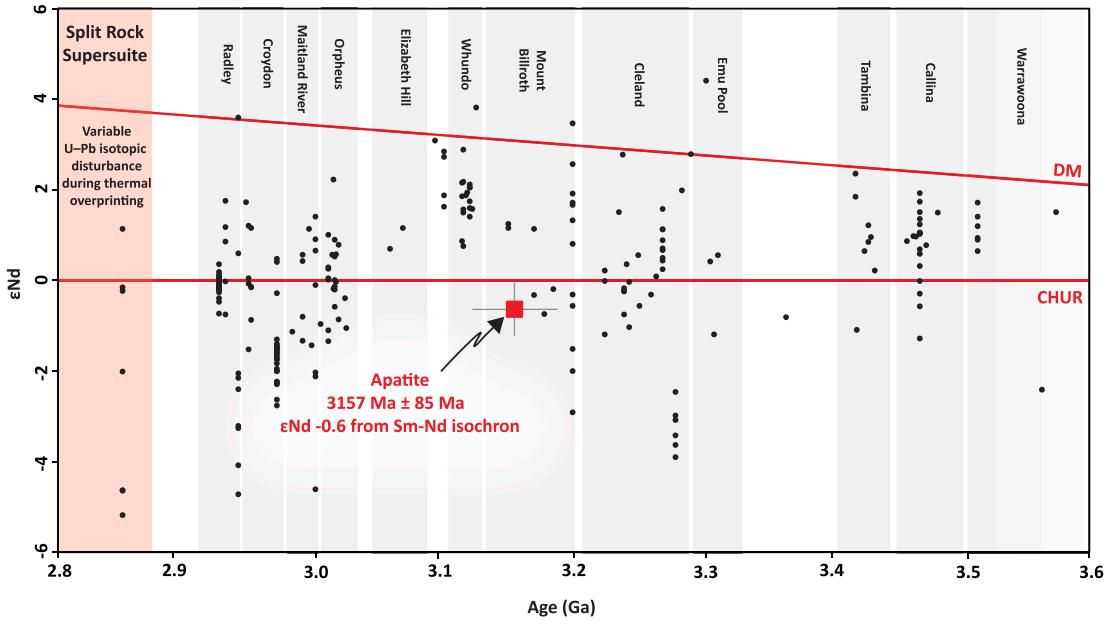

Fig. 7. εNd evolution plot versus indicated age. The red overlaid square is derived from detrital apatite Sm/Nd analysis. Whole-rock Nd values (black circles) were collected from crystalline basement lithologies of the Pilbara Craton (GSWA, 2023). Magmatic supersuites are labelled.

Shaw Rivers (de Laeter and Blockley, 1972) and has been dated via zircon U–Pb to c. 2.83 Ga, thus representing some of the youngest magmatism in the East Pilbara Terrane (GSWA, 2023). The Moolyella monzogranite intrudes the Bishop Creek monzonite, while the related 2.83 Ga Cooglegong monzogranite intrudes the Shaw granitic complex (from where sample 26, which gave 21 % of apatite U–Pb analyses, was collected) (de Laeter and Blockley, 1972). We conclude that the ^{207}Pb-corrected age probability maximum at c. 2912 Ma likely records the thermal overprinting of various apatite populations, resetting their Pb isotopic system during the discontinuous c. 2.89 to 2.83 (Hickman, 2021) emplacement of the Split Rock Supersuite. Such thermal disturbance of apatite is reflected in the U–Pb regression lines calculated for each sample (Fig. 4). MSWD values of >1 imply that a single age population does not define the calculated U–Pb mean age. The older lower intercept age obtained from sample 19 of 3087 ± 38, along with its more heterogenous Eu* signature, is distinct compared to samples 18 and 26 (Fig. 4). The latter two samples (18 and 26) share similar lower intercept ages of 2898 ± 28 Ma and 2834 ± 20 Ma, respectively, with similar Eu* values despite being over 80 km apart and located on distinct underlying lithologies (Fig. 4; Table 1). Based on Lu–Hf and Sm–Nd ratios that imply crystallisation ages which match the underlying crystalline basement, we interpret the detrital apatite to represent material derived out of proximal granitoids (Fig. 5). Consequently, the various isotopic signatures retained within the detrital apatite should reflect the thermal history of its source rock, consistent with the variable degrees of U–Pb resetting in these grains. Samples 18 and 26 are ~1.6 and 2.2 km from the Split Rock Supersuite plutons, whereas sample 19 is over 12 km from the nearest outcrop. Hence, we posit that the younger U–Pb lower intercept ages and more homogeneous Eu*signatures in samples 18 and 26 reflect higher degrees of thermal overprinting and recrystallisation (Berger et al., 2022; Kirkland et al., 2018).

Trace element geochemistry undertaken during Sm–Nd analysis can help enhance provenance interpretations (Fig. 7). Apatites from more felsic magmas typically have larger Eu anomalies, reflecting co-crystallisation with plagioclase (Mao et al., 2016). The mean Eu anomaly ($Eu/Eu^* = Eu_{CN}/(Sm_{CN} * Gd_{CN})^{-0.5}$) of the detrital apatite population is 0.73 (Fig. 4), a weakly negative signature, consistent with an intermediate melt source where the Eu^{2+} budget was not significantly depleted during prolonged plagioclase fractionation (Belousova et al., 2002; Buzenchi et al., 2022). The constituent lithologies of the Mt. Edgar Dome all demonstrate a negative Eu anomaly (Buzenchi et al., 2022). We interpret the Eu anomalies obtained for each sample (Fig. 4) to reflect the composition of the underlying granitoids variably modified by thermal/fluid overprinting during Split Rock granitoid emplacement (Fig. 4). Further, apatite εNd values define a normal distribution (Shapiro-Wilk = 0.85 and Anderson-Darling = 9.57 normality tests) about a CHUR-like composition with a mean of −0.6. This mean apatite Nd isotopic composition is similar to the average for granitoids within the EPT, which during the Mesoarchean have whole rock εNdi values that range between to −8 to +3 (Fig. 7) (GSWA, 2023).

5.2. Archean crust

5.2.1. The detrital record of crustal evolution

The detrital Hf pattern is generally very similar to that seen in the crystalline igneous record (Fig. 8C). εHf signatures for dominant detrital pulses at 3.45 and 3.30 Ga appear to reflect, on average, a greater degree of mixing with a radiogenic component than the earlier 3.60 Ga event, as preserved by zircon xenocrysts (Kemp et al., 2015; Petersson et al., 2019b). Such a mixing process could occur during pulses of magmatism associated with granitoid dome emplacement and greenstone subsidence (Fig. 8C; Fig. 9) (Roberts and Tikoff, 2021). The isotopic pattern for the Archean detrital grains is consistent with an autochthonous source, given that all data seem to originate from a common isotopic precursor compositionally indistinguishable from CHUR (based on Hf and Nd) at ≤ 3.8 Ga, consistent with the known crystalline igneous record (Gardiner et al., 2017; Petersson et al., 2019b) (Fig. 8C).

The crustal evolution of the Pilbara Craton is marked by magmatic events at c. 3.50, c. 3.43, 3.31, and 3.20 Ga, associated with the voluminous emplacement of granitoid domes (GSWA, 2023; Kemp et al., 2023; Petersson et al., 2020). One scenario to account for the quasiperiodic nature of crust formation, with an approximate rejuvenation period of 100 Ma, seen in the East Pilbara Terrane, is that of early-Archean crust formation being controlled by a series of gravitationally driven crustal overturns (François et al., 2014; Wiemer et al., 2018). In this model, high geothermal gradients in the Archean encouraged vertical material flow whereby denser mafic volcanics and lighter felsic crust could overturn on a quasiperiodic basis (Wiemer et al., 2018). Such vertical tectonic process is reflected in the architecture of the East Pilbara Terrane, where buoyant granitoid domes are bounded by denser keels of coeval komatiite successions in the greenstone belts (Petersson et al., 2020). Alternative tectonomagmatic scenarios are, however, proposed (Van Kranendonk et al., 2004), including initial crust formation in the East Pilbara Terrane as early as the Hadean (Tessalina et al., 2010), although this appears inconsistent with recent isotopic studies (Hartnady et al., 2022; Kemp et al., 2015; Kemp et al., 2023; Petersson et al., 2020).

A c. 100 Ma interval for rejuvenation events has been observed in the geology of other Archean terranes, such as the Kaapvaal Craton (Bédard, 2018) and the North Atlantic Craton, as expressed in West Greenland (Kirkland et al., 2021) (Fig. 8D). We propose that this cyclicity could appear as a characteristic feature of continental crust formation within the East Pilbara Terrane during the early Archean and may typify proto-crust development prior to modern-style plate tectonics (Wiemer et al., 2018). The c. 100 Ma interval may represent the time required for heat and volatiles to accumulate beneath stagnant lids to trigger voluminous magmatism associated with overturns events (Bédard, 2018).

Hence, our detrital zircon εHf data appears to reflect the quasiperiodic nature of crust formation on an approximate 100 Ma frequency (Fig. 8D). Whilst a c. 100 Ma frequency may characterise early Earth overturn processes, it need not be expected to be globally synchronous (e.g. the periodicity is the same across different cratons, but the specific initiation timing is distinct). We interpret the isotopic arrays to represent evolution with discrete periods of crustal reworking precipitated by a magmatic component with more radiogenic compositions, as marked by vertical εHf mixing arrays at 3.45 and 3.30 Ga, which, in both cases, extended into unradiogenic compositions similar to 3.6 Ga magmatism. These magmatic episodes define periods of crust generation (Hickman and Van Kranendonk, 2012; Van Kranendonk et al., 2004; Wiemer et al., 2018) (Fig. 8C).

5.2.2. Ancient crust unroofing

The granitoid domes of the East Pilbara Terrane are composite structures (Fig. 1) (Fig. 9) (Hickman, 2021; Roberts and Tikoff, 2021), in which pre-existing lithologies were destroyed (consumed/assimilated within new melts and also uplifted and eroded) during later granitoid emplacement – hence there is a progressively more limited igneous archive of early crust preserved in the Pilbara Craton. A consequence of this process is a trend from more radiogenic εHf positive values at the margins to less radiogenic, negative εHf values in the cores of the granitoid domes of the East Pilbara Terrane (Fig. 9) (Gardiner et al., 2017). The spatial zonation of εHf reflects this multi-stage formation of domes whereby the source melts become less radiogenic through the Archean, reflecting the increased incorporation of earlier reworked crust over more radiogenic melts (Fig. 8C) (Buzenchi et al., 2022; Gardiner et al., 2017).

Previous work in the East Pilbara Terrane has supported the existence of a poorly resolved and perhaps locally reworked (+ve εHf) proto-crust with an age of at least 3.55–3.80 Ga (Collins et al., 1998; Gardiner et al., 2017; Hickman, 1990; Hickman and Van Kranendonk, 2012; Petersson et al., 2019b). Indeed, recent insights from Pb isotopes in the Pilbara have demonstrated that continental nuclei derived from a

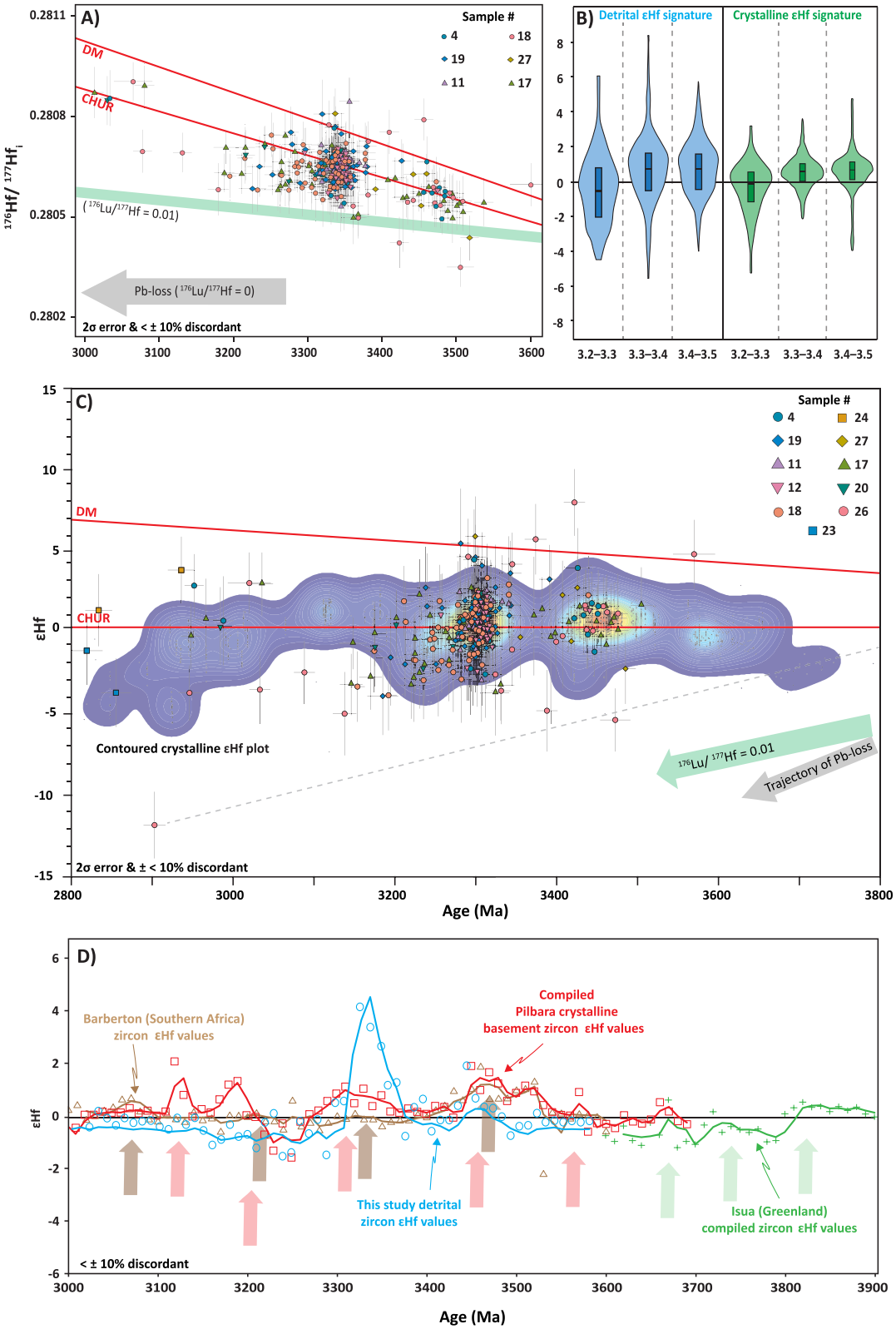

Fig. 8. (A) Initial $^{176}Hf/^{177}Hf$ versus concordia age of Archean detrital zircons (this study) with the expected trajectory for Pb-loss shown. A $^{176}Lu/^{177}Hf$ ratio of 0.01 for average Archean TTGs composition is also shown. (Blichert-Toft and Albarède, 2008; Taylor and McLennan, 1985). (B) Violin plots for the detrital εHf signatures compared to crystalline values from the East Pilbara Terrane. A list of data sources is available in Appendix 1. (C) εHf versus concordia age for detrital zircon. At least two vertical Hf mixing arrays (3.45 and 3.30 Ga) punctuate evolution slopes ($^{176}Lu/^{177}Hf = 0.01$). Hafnium data for contoured plot from Amelin et al. (2000); Gardiner et al. (2017); Kemp et al. (2015); Kemp et al. (2023); Petersson et al. (2020); Petersson et al. (2019b); Salerno et al. (2021). (D) A compilation of εHf values from various Archean terranes (interpolated on a 10 Ma interval with a 3-period moving average). Significant juvenile input events are highlighted. Hf data compiled from Puetz et al. (2021).

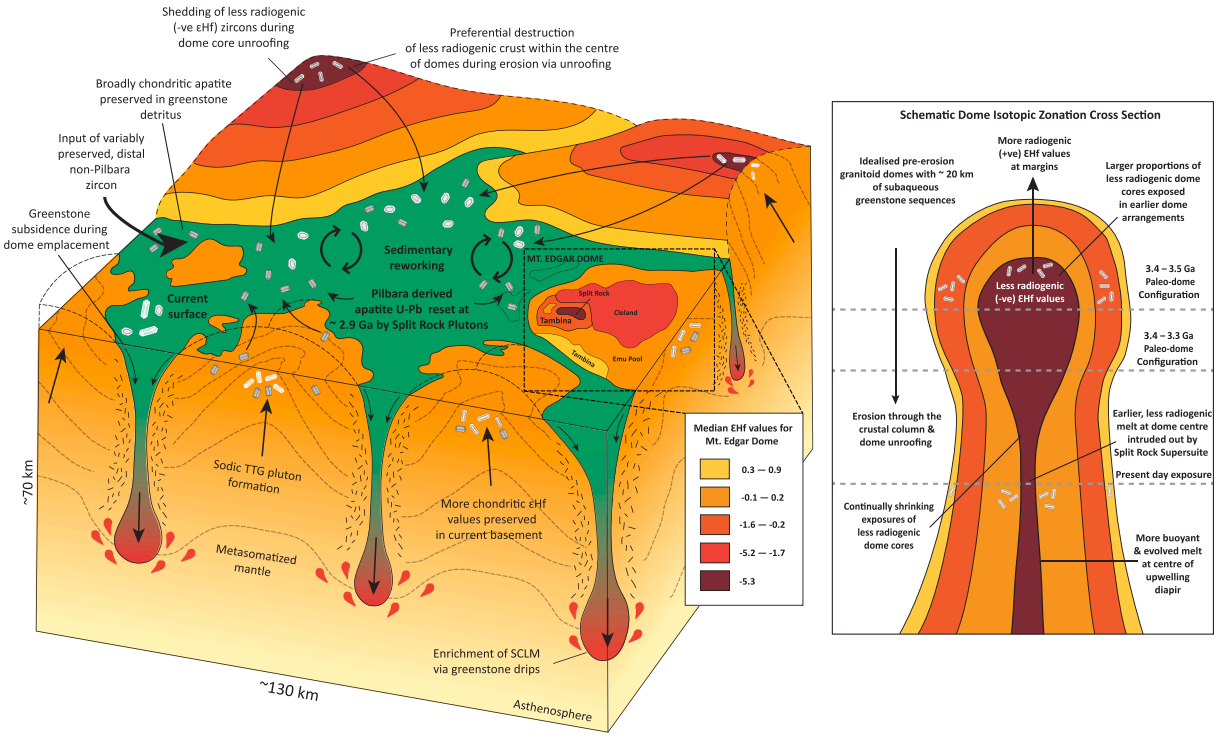

Fig. 9. Schematic block diagram of the East Pilbara Terrane showing the present surface and the hypothesised pre-erosion surface. Inputs of apatite and zircon off the denuded craton are indicated. A simplified εHf map of the Mount Edgar Dome, subdivided by magmatic supersuite and coloured by median εHf signature, highlights the general rim-core trend from more to less radiogenic compositions. Inset is a schematic cross-section of a granitoid dome, showing isotopic zonation. The εHf map was adapted after Gardiner et al. (2017). Block diagram adapted after Smithies et al. (2021).

CHUR-like source were preserved for up to 500 Ma following their formation during the Eoarchean to Paleoarchean, but not Hadean (Hartnady et al., 2022). This earlier crust has been studied indirectly through Nd and Hf model ages; however, direct insights have been limited to xenocrystic zircon crystals inherited within granitic gneiss or mafic enclaves within granitoids (Petersson et al., 2019a). Our εHf data may help resolve an earlier (≥3.8 Ga) crustal evolution array, as suggested in Hickman and Van Kranendonk (2012), Petersson et al. (2019a), and Hartnady et al. (2022). The fit of the lowermost isotopic evolution array through εHf data in Fig. 8C, using a $^{176}Lu/^{177}Hf$ of 0.01, appears to represent a preserved remnant of the continued isotopic evolution of an extraction event at c. 3.8 Ga (Petersson et al., 2019a) (Fig. 8C). Despite some of the less radiogenic εHf values in Petersson et al. (2019a) being interpreted as modified by radiogenic Pb-loss, the detrital data here and the K-feldspar Pb isotopic modelling of Hartnady et al. (2022) imply a real source component of up to 3.8 Ga. Such a 3.8 Ga source appears to coincide with more widespread crustal extraction or the better preservation of this isotopic legacy of fractionation after a putative late heavy bombardment (Drabon et al., 2022; Dröllner et al., 2022).

The Split Rock Suite (2.89–2.83 Ga) (Hickman, 2021) is the least radiogenic (−ve εHf) constituent of the Mt. Edgar dome (Gardiner et al., 2017) and is presently the least exposed supersuite by surface area (Fig. 9). Granitoid domes are multi-generational features whose younger cores extend from more radiogenic values into the same evolution array as the surrounding granitoid supersuites (Gardiner et al., 2017). The emplacement of granitoid domes in the EPT occurred via the upwelling of buoyant melt diapirs (Roberts and Tikoff, 2021; Wiemer et al., 2018) (Fig. 9). A 3-dimensional spatial isotopic arrangement within the paleo-domes could explain salient features within the detrital record. Specifically, if the paleo-domes had a proportionally greater volume of less radiogenic material higher within the crustal column, this would be preferentially eroded relative to more radiogenic and lower in the crustal column margins (Fig. 9). Such a process would result in zircon shed from central paleo-dome components having a bias towards less radiogenic (−ve) εHf, whilst zircons preserved within the crystalline basement would, on average,retain a more radiogenic (+ve) signature (Figs. 8B; 9). Despite similar median εHf values between detrital and magmatic zircons, the oldest detrital grains show a wider compositional range and encompass less radiogenic (−ve) εHf values. Critically, the interquartile range for the 3.5–3.4 Ga time interval encompasses proportionally more negative εHf values than the contemporaneous crystalline basement, supporting the described unroofing model (Fig. 8B).

The scattering of Archean zircon to lower εHf values due to radiogenic Pb-loss has been documented by previous workers (Petersson et al., 2019b; Spencer et al., 2020). Such a process could conceivably result in εHf trends that resemble those produced from the unroofing dome model presented (e.g. more unradiogenic signatures dominating the oldest detrital component). Some samples in this work yield a high percentage of discordant zircon grains (sample 26, 77 % are >10 % discordant), which we interpret as a function of grain antiquity, prolonged surficial exposure, bulk mounting and representative sampling. However, the % of discordant grains (i.e. increased radiogenic Pb-loss) does not increase over the 2.8–3.6 Ga interval and remains at a mean of ~22 % discordance (Appendix 2). Furthermore, Pb-loss is mitigated by filtering analyses with ± 10 % discordance, and no radiogenic Pb-loss trend is evident in εHf versus age plots where such a process yields a distinct vector (εHf/Ma = 0.022), which contrast to the observed trend in the data (Fig. 8). Hence, we attribute the distribution of data towards lower εHf values in old grains (Fig. 8B) as a function of a detrital process, whereby less radiogenic zircon grains in the dome cores are preferentially lost into the detrital archive following granitoid unroofing, given their concentric Hf (and Nd) isotopic zonation (Fig. 9).

The less radiogenic (−ve εHf) zircon shed from now-destroyed dome cores has been preserved proximally within basins to the East Pilbara Terrane (Fig. 9). Thus, the detrital record of the Pilbara may be a more extensive archive of the earlier, more evolved crust of the Pilbara Craton, in contrast to what the contemporary crystalline exposures offer.

6. Conclusions

New (U–Pb) time-constrained *in-situ* isotopic signatures (Lu–Hf, Sm–Nd) from detrital zircon and apatite grains collected from ephemeral streams offer insights into the construction and subsequent erosion of Archean continental crust. Zircon ages record a history of sediment flux into and within the Pilbara Craton.

Detrital zircon and apatite offer two distinct insights. The refractory and durable nature of zircon allows it to persist through multiple cycles of reworking. Detrital zircon grains record Pilbara magmatism but also represent an archive of Proterozoic and Phanerozoic geological history within Western Australia (e.g., Capricorn, Albany-Fraser, Paterson Orogens). The occurrence of young $\leq$ 500 Ma zircon grains also implies a detrital source into the Pilbara Craton from the Lhasa Block.

The labile nature of apatite is not conducive to prolonged transport, leading to a less diverse primary and, indeed, secondary age signature retained in this mineral. We record a unimodal apatite U–Pb age population at 2.9 Ga, interpreted as the time of thermal resetting due to heating from granitoids of the Split Rock Supersuite. While the Lu–Hf, (Eu/Eu*), and Sm–Nd isochrons constrain primary crystallisation primarily from the Bishop Creek Monzonite at c. 3.2 Ga and other granitoids of the EPT granitoid domes.

This work highlights a substantial geospatial control on zircon U–Pb age signatures, with samples collected directly atop granitoid domes showing a largely felsic mineral profile and unimodal age signatures, broadly corresponding to the dome's crystallisation (Fig. 1). Samples collected from greenstone terranes show a more heterogeneous age profile, retaining a greater number of younger grains, likely due to their lower intrinsic zircon load of the underlying basement.

Our detrital zircon εHf signatures, on average, stretch to more evolved values than previous data sets from crystalline samples of the domes (Fig. 8B). This observation supports an unroofing model, critically dependent on the observed age and isotopic zonation of the domes (youngest and least radiogenic in the dome cores). Detrital zircon potentially preserves information about lost components in the primary magmatic record and complements the crystalline record. However, the proportions of such ancient grains need not reflect volumetric proportions in the crystalline basement due to a plethora of geological (and analytical) biases imparted onto the DZ record.

The detrital zircon data (U–Pb, Lu–Hf) implies the continued reworking of earlier crustal components punctuated by the input of juvenile material on an approximate 100 Ma frequency, similar to some other ancient cratons (Fig. 8D). This reworking and periodic rejuvenation appear to occur quasiperiodically, perhaps during crust-mantle overturns.

This work shows that detrital apatite from ancient crust, due to its preservation potential and compositional growth affinity, will unlikely provide as extensive a crustal evolution record as detrital zircon. Nonetheless, detrital apatite in the Pilbara Craton offers important insights into thermal/fluid overprinting in the EPT poorly represented in the zircon record.

CRediT authorship contribution statement

Anthony J.I. Clarke: Investigation, Methodology, Visualization, Writing – original draft. **Christopher L. Kirkland:** Conceptualization, Investigation, Methodology, Supervision, Writing – review & editing. **Stijn Glorie:** Methodology, Supervision, Writing – review & editing. **Jack Gillespie:** Supervision, Writing – review & editing. **Peter D. Kinny:** Supervision, Writing – review & editing.

Declaration of Competing Interest

The authors declare that they have no known competing financial interests or personal relationships that could have appeared to influence the work reported in this paper.

Acknowledgments

This work was funded by an Australian Research Council Discovery Project (DP200101881). SG was supported by an Australian Research Council Future Fellowship (FT210100906). AC acknowledges helpful discussions with M. Dröllner, S. Makin and H. Olierook during data reduction and visualisation. GeoHistory Facility instruments in the JdLC, Curtin University, were funded via an Australian Geo-physical Observing System grant provided to AuScope Pty Ltd. by the AQ44 Australian Education Investment Fund program. AuScope and the Australian Government support the JdLC GeoHistory laser ablation facility through the National Collaborative Research Infrastructure Strategy. Bradley McDonald and Noreen Evans are thanked for their help with LA–ICP–MS analysis. This research was undertaken using the Tescan Mira3 TIMA with four PulsTor SDD X-ray detectors (ARC LE140100150) and Tescan Clara FESEM with Oxford Instruments Ultim Max 170 SDD X-ray detector, Symmetry EBSD detector and AZtec Synergy software (ARC LE190100176). We thank Wilson Teixeira and Elson Oliveira for their expeditious editorial handling. Tony Kemp, Allen Nutman and an anonymous reviewer, gave comments that significantly improved the quality of this work.

Appendix A. Supplementary material

Supplementary data to this article can be found online at https://doi.org/10.1016/j.precamres.2023.107132.

References

Amelin, Y., Lee, D.C., Halliday, A.N., 2000. Early-middle archaean crustal evolution deduced from Lu-Hf and U-Pb isotopic studies of single zircon grains. Geochim. Cosmochim. Acta 64, 4205–4225.

Barfod, G.H., Krogstad, E.J., Frei, R., Albarède, F., 2005. Lu-Hf and PbSL geochronology of apatites from Proterozoic terranes: A first look at Lu-Hf isotopic closure in metamorphic apatite. Geochim. Cosmochim. Acta 69, 1847–1859.

Barham, M., Kirkland, C.L., Handoko, A.D., 2022. Understanding ancient tectonic settings through detrital zircon analysis. Earth Planet. Sci. Lett. 583, 117425.

Bédard, Jean H., 2018. Stagnant lids and mantle overturns: Implications for Archaean tectonics, magmagenesis, crustal growth, mantle evolution, and the start of plate tectonics. Geosci. Front. 9 (1), 19–49. https://doi.org/10.1016/j.gsf.2017.01.005. ISSN 1674-9871.

Belousova, E., Griffin, W.L., O'Reilly, S.Y., Fisher, N., 2002. Apatite as an indicator mineral for mineral exploration: Trace-element compositions and their relationship to host rock type. J. Geochem. Explor. 76, 45–69.

Belousova, E., Kostitsyn, Y.A., Griffin, W.L., Begg, G.C., O'Reilly, S.Y., Pearson, N.J., 2010. The growth of the continental crust: Constraints from zircon Hf-isotope data. Lithos 119, 457–466.

Berger, A., Egli, D., Glotzbach, C., Valla, P.G., Pettke, T., Herwegh, M., 2022. Apatite low-temperature chronometry and microstructures across a hydrothermally active fault zone. Chem. Geol. 588, 120633.

Bickle, M., Morant, P., Bettenay, L., Boulter, C., Blake, T., Groves, D., 1985. Archaean tectonics of the Shaw Batholith, Pilbara Block, Western Australia: structural and metamorphic tests of the batholith concept. Evol. Archean Supracrustal Sequences 28, 325–341.

Blichert-Toft, J., Albarède, F., 2008. Hafnium isotopes in Jack Hills zircons and the formation of the Hadean crust. Earth Planet. Sci. Lett. 265, 686–702.

Buzenchi, A., Moreira, H., Dhuime, B., 2022. Evidence for Protracted Intracrustal Reworking of Palaeoarchaean Crust in the Pilbara Craton (Mount Edgar Dome, Western Australia). Lithosphere 2022.

Cawood, P.A., Hawkesworth, C.J., Dhuime, B., 2012. Detrital zircon record and tectonic setting. Geology 40, 875–878.

Cawood, P.A., Hawkesworth, C.J., Dhuime, B., 2013. The continental record and the generation of continental crust. GSA Bull. 125, 14–32.

Cherniak, D.J., 2000. Rare earth element diffusion in apatite. Geochim. Cosmochim. Acta 64, 3871–3885.

Chew, D.M., Spikings, R.A., 2015. Geochronology and thermochronology using apatite: time and temperature, lower crust to surface. Elements 11, 189–194.

Chew, D.M., Petrus, J.A., Kamber, B.S., 2014. U-Pb LA–ICPMS dating using accessory mineral standards with variable common Pb. Chem. Geol. 363, 185–199.

Chew, D.M., Spikings, R.A., 2021. Apatite U-Pb thermochronology: a review. Minerals 11, 1095.

Chew, D.M., Sylvester, P.J., Tubrett, M.N., 2011. U-Pb and Th–Pb dating of apatite by LA-ICPMS. Chem. Geol. 280, 200–216.

Chu, N.C., Taylor, R.N., Chavagnac, V., Nesbitt, R.W., Boella, R.M., Milton, J.A., German, C.R., Bayon, G., Burton, K., 2002. Hf isotope ratio analysis using multi-collector inductively coupled plasma mass spectrometry: an evaluation of isobaric interference corrections. J. Anal. At. Spectrom 17, 1567–1574.

Cochrane, R., Spikings, R.A., Chew, D.M., Wotzlaw, J.F., Chiaradia, M., Tyrrell, S., Schaltegger, U., Van der Lelij, R., 2014. High temperature (>350°C) thermochronology and mechanisms of Pb loss in apatite. Geochim. Cosmochim. Acta 127, 39–56.
Collins, W.J., Van Kranendonk, M.J., Teyssier, C., 1998. Partial convective overturn of Archaean crust in the east Pilbara Craton, Western Australia: driving mechanisms and tectonic implications. J. Struct. Geol. 20, 1405–1424.
Compston, W., 1999. Geological age by instrumental analysis: the 29th Hallimond Lecture. Mineral. Mag. 63, 297–311.
Coyner, S., Kamenov, G., Mueller, P., Rao, V., Foster, D., 2004. FC1: a Zircon Reference Standard for the Determination of Hf Isotopic Compositions via Laser Ablation ICP-MS. AGU Fall Meeting Abstracts.
Craddock, J.P., Ojakangas, R.W., Malone, D.H., Konstantinou, A., Mory, A., Bauer, W., Thomas, R.J., Affinati, S.C., Pauls, K., Zimmerman, U., Botha, G., Rochas-Campos, A., Santos, P.R., Tohver, E., Riccomini, C., Martin, J., Redfern, J., Horstwood, M., Gehrels, G., 2019. Detrital zircon provenance of Permo-Carboniferous glacial diamictites across Gondwana. Earth Sci. Rev. 192, 285–316.
de Laeter, J.R., Blockley, J.G., 1972. Granite ages within the Archaean Pilbara Block, Western Australia. J. Geol. Soc. Aust. 19, 363–370.
Dhuime, B., Hawkesworth, C.J., Cawood, P.A., Storey, C.D., 2012. A change in the geodynamics of continental growth 3 billion years ago. Science 335, 1334–1336.
Dhuime, B., Wuestefeld, A., Hawkesworth, C.J., 2015. Emergence of modern continental crust about 3 billion years ago. Nat. Geosci. 8, 552–555.
Dhuime, B., Hawkesworth, C.J., Delavault, H., Cawood, P.A., 2017. Continental growth seen through the sedimentary record. Sed. Geol. 357, 16–32.
Drabon, N., Byerly, B.L., Byerly, G.R., Wooden, J.L., Wiedenbeck, M., Valley, J.W., Kitajima, K., Bauer, A.M., Lowe, D.R., 2022. Destabilization of long-lived hadean protocrust and the onset of pervasive hydrous melting at 3.8 Ga. AGU Adv. 3, e2021AV000520.
Dröllner, M., Barham, M., Kirkland, C.L., 2023. Reorganization of continent-scale sediment routing based on detrital zircon and rutile multi-proxy analysis. Basin Res. 35, 363–386.
Dröllner, M., Kirkland, C.L., Barham, M., Evans, N.J., McDonald, B.J., 2022. A persistent Hadean–Eoarchean protocrust in the western Yilgarn Craton, Western Australia. Terra Nova n/a.
Dumitru, T.A., 2016. A New Zircon Concentrating Table Designed for Geochronologists, American Geophysical Union. AGU Fall Meeting Abstracts, San Francisco, pp. 23–2956.
Fisher, C.M., Vervoort, J.D., DuFrane, S.A., 2014a. Accurate Hf isotope determinations of complex zircons using the "laser ablation split stream" method. Geochem. Geophys. Geosyst. 15, 121–139.
Fisher, C.M., Vervoort, J.D., Hanchar, J.M., 2014b. Guidelines for reporting zircon Hf isotopic data by LA-MC-ICPMS and potential pitfalls in the interpretation of these data. Chem. Geol. 363, 125–133.
Fisher, C.M., Bauer, A.M., Luo, Y., Sarkar, C., Hanchar, J.M., Vervoort, J.D., Tapster, S.R., Horstwood, M., Pearson, D.G., 2020. Laser ablation split-stream analysis of the Sm-Nd and U-Pb isotope compositions of monazite, titanite, and apatite – Improvements, potential reference materials, and application to the Archean Saglek Block gneisses. Chem. Geol. 539.
François, C., Philippot, P., Rey, P., Rubatto, D., 2014. Burial and exhumation during Archean sagduction in the East Pilbara Granite-Greenstone Terrane. Earth Planet. Sci. Lett. 396, 235–251.
Gardiner, N.J., Hickman, A.H., Kirkland, C.L., Lu, Y., Johnson, T., Zhao, J.-X., 2017. Processes of crust formation in the early Earth imaged through Hf isotopes from the East Pilbara Terrane. Precambr. Res. 297, 56–76.
Gardiner, N.J., Maidment, D.W., Kirkland, C.L., Bodorkos, S., Smithies, R.H., Jeon, H., 2018. Isotopic insight into the Proterozoic crustal evolution of the Rudall Province, Western Australia. Precambr. Res. 313, 31–50.
Gillespie, J., Glorie, S., Khudoley, A., Collins, A.S., 2018. Detrital apatite U-Pb and trace element analysis as a provenance tool: Insights from the Yenisey Ridge (Siberia). Lithos 314–315, 140–155.
Gillespie, J., Kirkland, C.L., Kinny, P.D., Simpson, A., Glorie, S., Rankenburg, K., 2022. Lu–Hf, Sm–Nd, and U-Pb isotopic coupling and decoupling in apatite. Geochim. Cosmochim. Acta 338, 121–135.
Glorie, S., Gillespie, J., Simpson, A., Gilbert, S., Khudoley, A., Priyatkina, N., Hand, M., Kirkland, C.L., 2022. Detrital apatite Lu–Hf and U-Pb geochronology applied to the southwestern Siberian margin. Terra Nova 34, 201–209.
GSWA, 2023. Compilation of WAROX data : [Western Australia]/Government of Western Australia, Geological Survey of Western Australia. In: Peng, J., White, S.R. (Eds.). Geological Survey of Western Australia, East Perth, Western Australia.
Haines, P.W., Wingate, M., Kirkland, C.L., 2013. Detrital Zircon U–Pb Ages from the Paleozoic of the Canning and Officer Basins, Western Australia: Implications for Provenance and Interbasin Connections.
Hartnady, M.I.H., Kirkland, C.L., Smithies, R.H., Johnson, S.P., Johnson, T.E., 2022. Pb isotope insight into the formation of the Earth's first stable continents. Earth Planet. Sci. Lett. 578.
Hartnady, M.I.H., Kirkland, C.L., Martin, L., Clark, C., Smithies, R.H., Spaggiari, C.V., 2019. Zircon oxygen and hafnium isotope decoupling during regional metamorphism: implications for the generation of low $\delta^{18}O$ magmas. Contrib. Miner. Petrol. 175, 9.
Hartnady, M.I.H., Kirkland, C.L., 2019. A gradual transition to plate tectonics on Earth between 3.2 to 2.7 billion years ago. Terra Nova 31, 129–134.
Hawkesworth, C., Cawood, P.A., Dhuime, B., 2019. Rates of generation and growth of the continental crust. Geosci. Front. 10, 165–173.
Hawkesworth, C., Cawood, P.A., Dhuime, B., 2020. The evolution of the continental crust and the onset of plate tectonics. Front Earth Sci (Lausanne) 8.
Herrmann, M., Söderlund, U., Scherstén, A., Næraa, T., Holm-Alwmark, S., Alwmark, C., 2021. The effect of low-temperature annealing on discordance of U-Pb zircon ages. Sci. Rep. 11, 7079.
Hickman, A.H., 2021. East Pilbara Craton: A Record of one Billion Years in the Growth of Archean Continental Crust. Geological Survey of Western Australia, Perth.
Hickman, A.H., Van Kranendonk, M.J., 2012. Early Earth evolution: Evidence from the 3.5-1.8 Ga geological history of the Pilbara region of Western Australia. Episodes 35, 283–297.
Hickman, A.H., 1990. Geology of the Pilbara Craton. In: Glover, J.S., Myers, J.R., Ho, J.E. (Eds.), Third International Archaean Symposium Excursion Guidebook University of Western Australia, Perth, pp. 1–13.
Hocking, R.M., Langford, R.L., Thorne, A.M., Sanders, A.J., Morris, P.A., Strong, C.A., Gozzard, J.R., Riganti, A., 2001. A Classification System for Regolith in Western Australia. Geological Survey of Western Australia, Perth.
Jackson, S.E., Pearson, N.J., Griffin, W.L., Belousova, E.A., 2004. The application of laser ablation-inductively coupled plasma-mass spectrometry to in situ U-Pb zircon geochronology. Chem. Geol. 211, 47–69.
Jahn, I., Clark, C., Reddy, S., Taylor, R.J.M., 2021. Zircon U-Pb geochronology and Hf–O isotope characteristics of granitoids from the Capricorn Orogen, Western Australia. J. Petrol. 62.
Jahn, B.M., Glikson, A.Y., Peucat, J.J., Hickman, A.H., 1981. REE geochemistry and isotopic data of Archean silicic volcanics and granitoids from the Pilbara Block, Western Australia: implications for the early crustal evolution. Geochim. Cosmochim. Acta 45, 1633–1652.
Johnson, S.P., Korhonen, F.J., Kirkland, C.L., Cliff, J.B., Belousova, E.A., Sheppard, S., 2017. An isotopic perspective on growth and differentiation of Proterozoic orogenic crust: From subduction magmatism to cratonization. Lithos 268–271, 76–86.
Kemp, A.I.S., Hickman, A.H., Kirkland, C.L., Vervoort, J.D., 2015. Hf isotopes in detrital and inherited zircons of the Pilbara Craton provide no evidence for Hadean continents. Precambr. Res. 261, 112–126.
Kemp, A.I.S., Vervoort, J.D., Bjorkman, K.E., Iaccheri, L.M., 2017. Hafnium Isotope Characteristics of Palaeoarchaean Zircon OG1/OGC from the Owens Gully Diorite, Pilbara Craton, Western Australia. Geostand. Geoanal. Res. 41, 659–673.
Kemp, A.I.S., Vervoort, J.D., Petersson, A., Smithies, R.H., Lu, Y., 2023. A linked evolution for granite-greenstone terranes of the Pilbara Craton from Nd and Hf isotopes, with implications for Archean continental growth. Earth Planet. Sci. Lett. 601, 117895.
Kinny, P.D., Clark, C., Kirkland, C.L., Hartnady, M., Gillespie, J., Johnson, T.E., McDonald, B., 2022. How old are the Jack Hills metasediments really?: The case for contamination of bedrock by zircon grains in transported regolith. Geology 50, 721–725.
Kirkland, C.L., Hartnady, M.I.H., Barham, M., et al., 2021. Widespread reworking of Hadean-to-Eoarchean continents during Earth's thermal peak. Nat. Commun. 12, 331. https://doi.org/10.1038/s41467-020-20514-4.
Kirkland, C.L., Johnson, S.P., Smithies, R.H., Hollis, J.A., Wingate, M.T.D., Tyler, I.M., Hickman, A.H., Cliff, J.B., Tessalina, S., Belousova, E.A., Murphy, R.C., 2013a. Not-so-suspect terrane: Constraints on the crustal evolution of the Rudall Province. Precambr. Res. 235, 131–149.
Kirkland, C.L., Smithies, R.H., Woodhouse, A.J., Howard, H.M., Wingate, M.T.D., Belousova, E.A., Cliff, J.B., Murphy, R.C., Spaggiari, C.V., 2013b. Constraints and deception in the isotopic record; the crustal evolution of the west Musgrave Province, central Australia. Gondw. Res. 23, 759–781.
Kirkland, C.L., Yakymchuk, C., Szilas, K., Evans, N., Hollis, J., McDonald, B., Gardiner, N. J., 2018. Apatite: a U-Pb thermochronometer or geochronometer? Lithos 318–319, 143–157.
Korenaga, J., 2013. Initiation and Evolution of Plate Tectonics on Earth: Theories and Observations. Annu. Rev. Earth Planet. Sci. 41, 117–151.
Lewis, C., Sircombe, K., 2013. Use of U-Pb geochronology to delineate provenance of North West Shelf Sediments, Australia.
Li, Y., Vermeesch, P., 2021. Short communication: Inverse isochron regression for Re–Os, K-Ca and other chronometers. Geochronology 3, 415–420.
Malusà, M.G., Resentini, A., Garzanti, E., 2016. Hydraulic sorting and mineral fertility bias in detrital geochronology. Gondw. Res. 31, 1–19.
Mao, M., Rukhlov, A.S., Rowins, S.M., Spence, J., Coogan, L.A., 2016. Apatite Trace Element Compositions: A Robust New Tool for Mineral Exploration. Econ. Geol. 111, 1187–1222.
Marsh, J.H., Jørgensen, T.R.C., Petrus, J.A., Hamilton, M.A., Mole, D.R., 2019. U-Pb, trace element, and hafnium isotope composition of the Maniitsoq zircon: A potential new Archean zircon reference material. Goldschmidt, Barcalona.
Martin, E.L., Collins, W.J., Kirkland, C.L., 2017. An Australian source for Pacific-Gondwanan zircons: Implications for the assembly of northeastern Gondwana. Geology 45, 699–702.
Moecher, D., Samson, S., 2006. Differential zircon fertility of source terranes and natural bias in the detrital zircon record: Implications for sedimentary provenance analysis. Earth Planet. Sci. Lett. 247, 252–266.
Morel, M.L.A., Nebel, O., Nebel-Jacobsen, Y., Miller, J., Vroon, P.Z., 2008. Hafnium isotope characterization of the GJ-1 zircon reference material by solution and laser-ablation MC-ICPMS. Chem. Geol. 255, 231–235.
Morón, S., Cawood, P.A., Haines, P.W., Gallagher, S.J., Zahirovic, S., Lewis, C.J., Moresi, L., 2019. Long-lived transcontinental sediment transport pathways of East Gondwana. Geology 47, 513–516.
Myers, J.S., 1993. Precambrian History of the West Australian Craton and Adjacent Orogens. Annu. Rev. Earth Planet. Sci. 21, 453–485.
Nelson, D., 2005. Compilation of geochronology data. June.

Nutman, A.P., Bennett, V.C., Friend, C.R.L., Polat, A., Hoffmann, E., Van Kranendonk, M., 2021. Fifty years of the Eoarchean and the case for evolving uniformitarianism. Precambr. Res. 367, 106442.
O'Sullivan, G., Chew, D.M., Kenny, G., Henrichs, I., Mulligan, D., 2020. The trace element composition of apatite and its application to detrital provenance studies. Earth-Sci. Rev. 201.
Petersson, A., Kemp, A.I.S., Hickman, A.H., Whitehouse, M.J., Martin, L., Gray, C.M., 2019a. A new 3.59 Ga magmatic suite and a chondritic source to the east Pilbara Craton. Chem. Geol. 511, 51–70.
Petersson, A., Kemp, A.I.S., Whitehouse, M.J., 2019b. A Yilgarn seed to the Pilbara Craton (Australia)? Evidence from inherited zircons. Geology 47, 1098–1102.
Petersson, A., Kemp, A.I.S., Gray, C.M., Whitehouse, M.J., 2020. Formation of early Archean Granite-Greenstone Terranes from a globally chondritic mantle: insights from igneous rocks of the Pilbara Craton, Western Australia. Chem. Geol. 551, 119757.
Pidgeon, R., Nemchin, A., Whitehouse, M.J., 2017. The effect of weathering on U-Th–Pb and oxygen isotope systems of ancient zircons from the Jack Hills, Western Australia. Geochim. Cosmochim. Acta 197, 142–166.
Puetz, S.J., Spencer, C.J., Ganade, C.E., 2021. Analyses from a validated global UPb detrital zircon database: Enhanced methods for filtering discordant UPb zircon analyses and optimizing crystallization age estimates. Earth Sci. Rev. 220, 103745.
Riebe, C.S., Sklar, L.S., Lukens, C.E., Shuster, D.L., 2015. Climate and topography control the size and flux of sediment produced on steep mountain slopes. Proc. Natl. Acad. Sci. 112, 15574–15579.
Roberts, N.M., Tikoff, B., 2021. Internal structure of the Paleoarchean Mt Edgar dome, Pilbara Craton, Western Australia. Precambr. Res. 358.
Salama, W., Anand, R.R., Tunmer, W., Aspandiar, M., 2022. Regolith characterization and landscape evolution for geochemical exploration of the covered Yamarna Terrane, Western Australia. J. Geochem. Explor. 232, 106881.
Salerno, R., Vervoort, J., Fisher, C., Kemp, A., Roberts, N., 2021. The coupled Hf-Nd isotope record of the early Earth in the Pilbara Craton. Earth Planet. Sci. Lett. 572.
Sandiford, M., Van Kranendonk, M.J., Bodorkos, S., 2004. Conductive incubation and the origin of dome-and-keel structure in Archean granite-greenstone terrains: a model based on the eastern Pilbara Craton, Western Australia. Tectonics 23.
Schmitz, M.D., Bowring, S.A., Ireland, T.R., 2003. Evaluation of Duluth Complex anorthositic series (AS3) zircon as a U-Pb geochronological standard: new high-precision isotope dilution thermal ionization mass spectrometry results. Geochim. Cosmochim. Acta 67, 3665–3672.
Schoene, B., Bowring, S., 2006. U-Pb systematics of the McClure Mountain syenite: Thermochronological constraints on the age of the $^{40}Ar/^{39}Ar$ standard MMhb. Contrib. Miner. Petrol. 151, 615–630.
Schoene, B., Bowring, S.A., 2007. Determining accurate temperature–time paths from U-Pb thermochronology: An example from the Kaapvaal craton, southern Africa. Geochim. Cosmochim. Acta 71, 165–185.
Simpson, A., Gilbert, S., Tamblyn, R., Hand, M., Spandler, C., Gillespie, J., Nixon, A., Glorie, S., 2021. In-situ Lu Hf geochronology of garnet, apatite and xenotime by LA ICP MS/MS. Chem. Geol. 577.
Sláma, J., Košler, J., Condon, D.J., Crowley, J.L., Gerdes, A., Hanchar, J.M., Horstwood, M.S.A., Morris, G.A., Nasdala, L., Norberg, N., Schaltegger, U., Schoene, B., Tubrett, M.N., Whitehouse, M.J., 2008. Plešovice zircon — A new natural reference material for U-Pb and Hf isotopic microanalysis. Chem. Geol. 249, 1–35.
Smithies, R.H., Lu, Y., Kirkland, C.L., Johnson, T.E., Mole, D.R., Champion, D.C., Martin, L., Jeon, H., Wingate, M.T.D., Johnson, S.P., 2021. Oxygen isotopes trace the origins of Earth's earliest continental crust. Nature 592, 70–75.
Spaggiari, C., Kirkland, C., Smithies, R., Occhipinti, S., Wingate, M., 2014. Geological framework of the Albany-Fraser Orogen, pp. 12–27.
Spencer, C.J., Cawood, P.A., Hawkesworth, C.J., Prave, A.R., Roberts, N.M.W., Horstwood, M.S.A., Whitehouse, M.J., 2015. Generation and preservation of continental crust in the Grenville Orogeny. Geosci. Front. 6, 357–372.
Spencer, C.J., Kirkland, C.L., Roberts, N.M.W., Evans, N.J., Liebmann, J., 2020. Strategies towards robust interpretations of in situ zircon Lu–Hf isotope analyses. Geosci. Front. 11, 843–853.
Stacey, J.S., Kramers, J.D., 1975. Approximation of terrestrial lead isotope evolution by a two-stage model. Earth Planet. Sci. Lett. 26, 207–221.
Stern, R.A., Bodorkos, S., Kamo, S.L., Hickman, A.H., Corfu, F., 2009. Measurement of SIMS Instrumental Mass Fractionation of Pb Isotopes During Zircon Dating. Geostand. Geoanal. Res. 33, 145–168.
Strong, T.R., Driscoll, R.L., 2016. A process for reducing rocks and concentrating heavy minerals, Open-File Report, Reston, VA.
Taylor, S.R., McLennan, S.M., 1985. The Continental Crust: Its Composition and Evolution. Blackwell Scientific Pub, Palo Alto, CA, United States.
Thomson, S.N., Gehrels, G.E., Ruiz, J., Buchwaldt, R., 2012. Routine low-damage apatite U-Pb dating using laser ablation–multicollector–ICPMS. Geochem. Geophys. Geosyst. 13.
Tucker, N.M., Morrissey, L.J., Payne, J.L., Szpunar, M., 2018. Genesis of the Archean-Paleoproterozoic Tabletop Domain, Rudall Province, and its endemic relationship to the West Australian Craton. Aust. J. Earth Sci. 65, 739–768.
Van Kranendonk, M.J., Collins, W.J., Hickman, A., Pawley, M.J., 2004. Critical tests of vertical vs. horizontal tectonic models for the Archaean East Pilbara Granite-Greenstone Terrane, Pilbara Craton, Western Australia. Precambr. Res. 131, 173–211.
Van Kranendonk, M.J., Smithies, R.H., Hickman, A.H., Champion, D.C., 2007a. Chapter 4.1 Paleoarchean Development of a Continental Nucleus: the East Pilbara Terrane of the Pilbara Craton, Western Australia. In: Van Kranendonk, M.J., Smithies, R.H., Bennett, V.C. (Eds.), Developments in Precambrian Geology. Elsevier, pp. 307–337.
Van Kranendonk, M.J., Smithies, R.H., Hickman, A.H., Champion, D.C., 2007b. Review: secular tectonic evolution of Archean continental crust: interplay between horizontal and vertical processes in the formation of the Pilbara Craton, Australia. Terra Nova 19, 1–38.
Van Kranendonk, M.J., 2008. Structural geology of the central part of the Lalla Rookh – Western Shaw structural corridor, Pilbara Craton,. In: Tetlaw, N.S. (Ed.). Geological Suvery of Western Australia, Perth, p. 29.
Veevers, J.J., Saeed, A., Belousova, E.A., Griffin, W.L., 2005. U-Pb ages and source composition by Hf-isotope and trace-element analysis of detrital zircons in Permian sandstone and modern sand from southwestern Australia and a review of the paleogeographical and denudational history of the Yilgarn Craton. Earth Sci. Rev. 68, 245–279.
Vermeesch, P., 2018. IsoplotR: A free and open toolbox for geochronology. Geosci. Front. 9, 1479–1493.
Wiemer, D., Schrank, C.E., Murphy, D.T., Wenham, L., Allen, C.M., 2018. Earth's oldest stable crust in the Pilbara Craton formed by cyclic gravitational overturns. Nat. Geosci. 11, 357–361.
Windley, B.F., Kusky, T., Polat, A., 2021. Onset of plate tectonics by the Eoarchean. Precambr. Res. 352, 105980.
Woodhead, J.D., Hergt, J.M., 2005. A Preliminary Appraisal of Seven Natural Zircon Reference Materials for In Situ Hf Isotope Determination. Geostand. Geoanal. Res. 29, 183–195.
Wopfner, H., Jin, X., 2009. Pangea Megasequences of Tethyan Gondwana-margin reflect global changes of climate and tectonism in Late Palaeozoic and Early Triassic times–A review. Palaeoworld 18, 169–192.
Yang, Y.H., Wu, F.Y., Yang, J.H., Chew, D.M., Xie, L.W., Chu, Z.Y., Zhang, Y.B., Huang, C., 2014. Sr and Nd isotopic compositions of apatite reference materials used in U-Th–Pb geochronology. Chem. Geol. 385, 35–55.
Zhu, D.C., Zhao, Z.D., Niu, Y., Dilek, Y., Mo, X.X., 2011a. Lhasa terrane in southern Tibet came from Australia. Geology 39, 727–730.
Zhu, D.C., Zhao, Z.D., Niu, Y., Mo, X.X., Chung, S.L., Hou, Z., Wang, L.Q., Wu, F.Y., 2011b. The Lhasa Terrane: Record of a microcontinent and its histories of drift and growth. Earth Planet. Sci. Lett. 301, 241–255.
Zutterkirch, I.C., Kirkland, C.L., Barham, M., Elders, C., 2021. Thin-section detrital zircon geochronology mitigates bias in provenance investigations. J. Geol. Soc. Lond. 179.